LASER & PHOTONICS REVIEWS

www.lpr-journal.org

Resolution Enhancement and Background Suppression in Optical Super-Resolution Imaging for Biological Applications

*Chuankang Li, Vannhu Le, Xiaona Wang, Xiang Hao, Xu Liu, and Cuifang Kuang**

For decades, the spatial resolution of conventional far-field optical imaging has been constrained due to the diffraction limit. The emergence of optical super-resolution imaging has facilitated biological research in the nanoscale regime. However, the existing super-resolution modalities are not feasible in many biological applications due to weaknesses, like complex implementation and high cost. Recently, various newly proposed techniques are advantageous in the enhancement of the system resolution, background suppression, and improvement of the hardware complexity so that the above-mentioned issues could be addressed. Most of these techniques entail the modification of factors, like hardware, light path, fluorescent probe, and algorithm, based on conventional imaging systems. Particularly, subtraction technique is an easily implemented, cost-effective, and flexible imaging tool which has been applied in widespread utilizations. In this review, the principles, characteristics, advances, and biological applications of these techniques are highlighted in optical super-resolution modalities.

1. Introduction

Due to the diffraction limit, the resolution of conventional optical microscopy in the far field is constrained to $\lambda/(2\mathrm{NA})$,[1] where λ is the illumination wavelength and NA is the numerical aperture of the image-capturing optics. Confocal laser scanning microscopy (CLSM) has been broadly applied to 3D specimen analysis and has become a routine tool for studying samples in the life sciences with relatively low out-of-focus background.[2,3] The pointwise scanning scheme of CLSM has improved spatial lateral resolution by a factor of $\sqrt{2}$. Because the dimensions of sub-cellular structures (like microfilament diameter), organelles (like lysosomes), virus, and proteins are normally beyond the resolving ability of conventional optics, the demand for a higher spatial resolution in optical microscopy has prompted the development of optical super-resolution imaging techniques that are capable of breaking this optical barrier.[4]

As is well known, Abbe's assumption is based on the conditions of linear light–matter interaction and single-image acquisition.[5,6] In order to achieve a sharper point spread function (PSF), patterned illumination is utilized in stimulated emission depletion microscopy (STED), in which one laser beam is modulated into doughnut-shaped profile featuring zero-intensity at the center.[7] The molecules in the laser foci will be registered to electron excited state due to the solid excitation beam. With the employment of the ultrahigh power radiation of doughnut-shaped beam, the molecules are quenched everywhere except the very center of focal spot due to stimulated emission effect.[8,9] STED microscopy is based on a confocal point-scanning scheme and a PSF-shrunken spot scans the region of interest (ROI), thereby obtaining super-resolved images. This strategy is quite enlightening that the two beams rather conspicuously aim to discriminate between the two molecular energy states in order to discern the molecular neighborhood in the proximity of the diffraction limit.[10] It should be noted that STED microscopy is limited by the inherent high intensity radiation which can potentially induce deleterious side effects such as photobleaching or phototoxicity.[11–13] In addition, another non-negligible limitation is the problem of strong background signals, mostly attributed to secondary excitation of the depletion beam.[14–19] The requirement of special dyes for STED is another drawback.[5] These disadvantages have given rise to the development of other STED-like sub-diffracted optical imaging techniques, such as saturated absorption competition microscopy,[20] charge state depletion microscopy (CSD),[21]

C. Li, Dr. V. Le, X. Wang, Prof. X. Hao, Prof. X. Liu, Prof. C. Kuang
State Key Laboratory of Modern Optical Instrumentation
College of Optical Science and Engineering
Zhejiang University
Hangzhou 310027, China
E-mail: cfkuang@zju.edu.cn

Dr. V. Le
Department of Optical Engineering
Le Quy Don Technical University
Hanoi 100803, Vietnam

Prof. X. Liu, Prof. C. Kuang
Collaborative Innovation Center of Extreme Optics
Shanxi University
Taiyuan 030006, China

Prof. C. Kuang
Ningbo Research Institute
Zhejiang University
Ningbo 315100, China

The ORCID identification number(s) for the author(s) of this article can be found under https://doi.org/10.1002/lpor.201900084

DOI: 10.1002/lpor.201900084

 © 2020 Wiley-VCH GmbH

fluorescence quenching microscopy (FQM),[22] excited state saturation microscopy (ESSat).[23]

Single-molecular localization microscopy (SMLM) is another kind of super-resolution strategy that involves the exploitation of molecular energy state differences and multiple-beam illumination, including techniques like stochastic optical reconstruction microscopy (STORM)[24] and photoactivated localization microscopy (PALM).[25] Through sequential wide-field illuminations, sparsely distributed molecules beyond the diffraction limit, are registered in each illumination, yielding a large quantity of image frames. Digital reconstruction of these images results in super-resolved biological structures. However, SMLM is constrained by disadvantages, like long acquisition time and the special probe requirement. Structured illumination microscopy (SIM) is an alternative based on patterned illumination and multiple-beam acquisition, which circumvents the diffraction barrier by a factor of 2.[26] Using periodic patterns with different illumination angles and polarization states, high frequency information can be extracted via postprocessing. However, this technique is costly due to expensive recording electronics in order to achieve video-rate acquisition speed.[5]

Although the aforementioned super-resolution imaging techniques are commercially available microscopic systems and are amenable to biological imaging, each technique has associated limitations which must be addressed before widespread applications. The drawbacks include highly complicated optical systems, specialized dyes, expensive instrumentation, high power sources, time-consuming data processing,[27] and the photodamage side-effect.[9] In order to ameliorate super-resolution systems either in resolution enhancement or SNR improvement, one or several factors in the following are routinely involved in the modification: hardware, light path, probes, and algorithm. For example, by replacing the single detector with the detector array and using photon reassignment algorithm, total improvement in resolution with a factor of 1.7 can be achieved compared with confocal microscopy.[6] Alternately, subtracting the confocal signals at different pinhole sizes yields doubling of the attainable spatial resolution with only minor modification of fluorescence detection component.[28,29] One conspicuous approach takes advantage of the physical expansion of fixed specimens using swellable polymer networks, which further extends the spatial resolution of SIM to ≈30 nm in visualization of microbial cytoskeleton structures.[30] Again, the uncorrelated background normally contaminates the image quality and degrades the final SNR during STED microscopic recording. The impact of photobleaching would rather make it difficult to realize high contrast measurement. By virtue of the background suppression techniques, like time-gating,[14] multibeam scanning,[16] or signal modulation,[15] background-free imaging becomes available. These approaches involve reducing background noise and they are applicable to other areas, like material sciences.[31] Deconvolution is another effective type of digital image processing algorithm which can provide good resolution enhancement up to a factor of 2 in STED microscopy.[32] However, the resolution obtained by the deconvolution process is strictly dependent on quality of the prior information introduced in the algorithm, such as the sample morphological properties and the PSF.

For decades, subtraction technique has been considered as a useful tool for enhancing spatial resolution and improving signal-to-noise ratio (SNR) in the fluorescence optical imaging system.[33] Note that almost all investigations related to differential techniques involve a subtraction between two or more corresponding elements. For example, during the process of the subtraction or differential, two images are required based on two different imaging conditions, such as two different illumination beams or two different detectors. The crucial aspect is to identify the differential elements (**Table 1**).[23] For example, in the time domain, lifetime distinction caused by high depletion intensity used in STED imaging can be utilized to separate diffraction-limited features.[17,34] In the intensity domain, two images acquired by using a Gaussian beam and a doughnut-shaped beam, respectively, can be processed based on intensity subtraction with certain coefficient values so that high-frequency signals can be extracted or background distribution can be suppressed.[35] Thus, the subtraction of one image from the other using a normalized subtraction coefficient yields an improved spatial resolution or SNR.

To date, the subtracting technique has the following advantages (Table 1). i) This technique is quite cost-effective compared with some hardware-based strategies, because it only involves the subtraction algorithm.[36] ii) The implementation is quite simple to be absent of precise realignment in light paths, so the required beam paths can be easily assembled in the laboratory.[37] iii) This technique is more suitable for in vivo imaging since it requires lower laser power, which minimizes photodamage of living specimens.[38] iv) It is able to increase penetration depth, especially in turbid tissues, like mouse brain.[39] v) No prior information is required in complex morphological specimens.[5] vi) Not constrained by special photoswitchable fluorophores, subtractive method helps to achieve single molecule localization imaging.[40] vii) It is advantageous for the removal of uncorrelated background, such as the autofluorescence in fluorescent labeled biological samples.[41–44] viii) Additionally, this approach can be applied to any laser scanning microscopy method, and is particularly useful for label-free imaging, where the common super resolution methods cannot be used.[45] Also, subtraction techniques have been adapted to a wide variety of applications, such as nanoscale 3D measurement,[46–48] quantum sensing,[49,50] photoacoustic imaging,[51,52] quantitative phase imaging,[53] lifetime imaging,[54] expansion microscopy,[55] differential interference contrast microscopy,[56] quantitative mass imaging, and so on.[57] Currently, subtraction methods have also been widely utilized to super-resolution microscopy and nonlinear optical imaging (NLO).[58–63]

There are few works that focus on this topic and present comprehensive discussions on this matter. As such, our work provides a systematic study of subtraction methods in the super-resolution imaging, including its theory, development, and applications (Figure S1, Supporting Information; Table 1), especially for the biological imaging (Figure S2, Supporting Information). The rest of this review is organized as several sections. Section 2 includes a discussion on several important concepts concerning imaging. Section 3 highlights the characteristics and advances of techniques that enhance resolution and reduce background in super-resolution imaging. Some vital factors in subtractive super-resolution imaging, like inorganic probes, acquisition speed, and axial resolution enhancement, are also summarized. Section 4 presents applications in other correlative imaging

© 2020 Wiley-VCH GmbH

Table 1. Overview of the subtractive super-resolution imaging methods and their specific parameters.

Imaging technique[a]	Subtractive method	Equation[b]	Optimal coefficient	Resolution[c]	2D/3D	Advantage[d]	Disadvantage[d]	Application	Reference
PSM	Intensity subtraction	$I_{sub} = I_{big} - \alpha I_{small}$ $I_{sub} = I_{small} - \alpha(I_{big} - I_{small})$ $I_{sub} = I_{pass} - \alpha I_{block}$ $I_{Ringn} = I_{Rawn} - \alpha I_{Rawn-1}$	0.76–0.88	$1/3.3\lambda$	2D,3D	Resolution enhancement	Low SNR	Optical sectioning	[28, 29, 69, 70, 234]
PMS	Phase subtraction	$g_{sub} = g_1 - \alpha g_2$ $g_{sub} = g_{dot} - \alpha g_{dark}$ $D_{VAE} = D_C - D_D$	0.6–0.9	$1/3.5\lambda$	2D	Extended depth of field	Multiparameter matching	Thick tissue imaging	[78, 79, 235]
WSM	Intensity subtraction	$FT(I2 - I1) = FT(I2) - FT(I1)$	/	/	2D	High speed and real time	/	Lensless coherent imaging	[80]
ISM	Pixel reassignment	$I_{sub} = I_{cent} - I_{peri}$	/	$1/3.5\lambda$	2D,3D	Flexible	Long acquisition time	Thick tissue imaging	[84, 87]
DA	Pixel reassignment Intensity subtraction	$h_{rec} = h_{pr} - \alpha I_{hollow}$ $I_{sub} = I_{ISM} - \alpha I_{wf}$ $I_{sub} = I_{ISM,outer} - \alpha I_{outer}$	/	$1/4\lambda$	2D,3D	Capable to correct aberration	Complexity in detector array	Thick tissue imaging	[91–93, 161]
vSAF	Near-field detection Intensity subtraction	$I_{vSAF} = I_{UAF+SAF} - I_{UAF}$	/	$1/6.7\lambda$	2D	No need of complex excitation	/	Thick tissue imaging	[81]
SO	Phase subtraction	$g_{sub} = g - \alpha g_{PM}$	0.65–0.75	$1/6\lambda$	2D	Decreased background noise	Nanoscale accuracy required	Low-sidelobe biological imaging	[231]
TIRF	Near-field detection Photobleaching of dyes	$I = I_n - I_{n+1}$ $(I = I_n - I_{n+2})$	/	$1/4\lambda$	3D	No constraint in special dyes	Severe influence of background noise	Thick tissue imaging	[83]
SSM	Vectorial beam Intensity subtraction	$I_{sub} = (I_x + I_y)/2 - \alpha\lvert I_x - I_y\rvert$ $I_{sub\text{-}AP} = I_{wf} - I_{conf\text{-}AP}$	0.5–0.66	$1/4\lambda$	2D	Only requirement for linear polarization	polarization-sensitive	DNA fragment observation	[95, 236]
SLAM	Vectorial beam Intensity subtraction	$I_{SLAM} = I_{bright} - \alpha I_{dark}$	/	$1/4.6\lambda$	2D	Label-free	Sample drift in live cell imaging	Compatible to SHG, THG, CARS	[96, 215]
cvFED	Vectorial beam Intensity subtraction	$I_{sub} = I_{flat} - I_{HAP}$ $I_{sub} = I_{RP} - I_{AP}$	0.4–0.5	$1/4\lambda$	2D	Largely reduced negative value	/	Living cell imaging	[103, 237]
sFED	Saturated absorption Intensity subtraction	$I_{sFED} = I_{ssolid} - \alpha I_{shollow}$	Weighted	$1/6\lambda$	2D	Largely reduced negative value	High risk of photodamage	Living cell samples	[108]
fFED	Pixel reassignment Phase subtraction	$I = I_{ISM} - \alpha I_{wf}$ $I = I_{ISM,outer} - \alpha I_{outer}$ $I_{FED} = I_{solid\_blue} - \alpha I_{hollow\_green}$ $I_{rec}(r') = I_{pr}(r') - \alpha I_{hollow}(r')$ $I_{wfFED} = I_{wf} - \alpha I_{lattice}$	0.95	$1/10\lambda$	2D,3D	Reduced deformation Fast imaging Prevention for sample drifting	/	Dynamic biological imaging	[91, 156, 161–163]
3dFED	Phase subtraction	$I_{3dFED} = I_c - \alpha I_{xy} - \gamma I_z$	0.7–1	$1/4\lambda$	3D	Axial resolution enhancement	/	3D living cell imaging	

(*Continued*)

© 2020 Wiley-VCH GmbH

Table 1. Continued.

*I*maging technique[a)]	Subtractive method	Equation[b)]	Optimal coefficient	Resolution[c)]	2D/3D	Advantage[d)]	Disadvantage[d)]	Application	Reference
SPCE-D	Vectorial beam Intensity subtraction	$I_{FED} = I_{solid} - \alpha I_{hollow}$ $I_{FED} = I_{off\text{-}focus} - \alpha I_{on\text{-}focus}$ $I_{FED} = I_{RP} - \alpha I_{CP}$	0.25	$1/4\lambda$	2D	No need of realignment	/	Morphological imaging in Nanomaterial	[71, 110–112]
CBS	Intensity subtraction	$I_{CBS} = I_{BB} - I_{CB}$	/	$1/2.9\lambda$	3D	Low scattering	Doubled light exposure	Dynamic biological imaging	[99]
gSTED	Lifetime separation	$I = I_{open} - I_{close}$ $I = I_{T1} - \alpha I_{T2}$	/	$1/12\lambda$	2D	Easy implementation	Hardware in lifetime module	Dynamic biological imaging	[14, 18, 130]
SPLIT	Lifetime separation	$I = I_{long} - \alpha I_{short}$ $N_1 = N - N_2 - N_{BKGD}$	0.5	/	2D	No need of prior information	Occurring on a faster time scale	Dynamic biological imaging	[17, 34]
mod-STED	Lock-in modulation	$I_{lock\text{-}in} = I_{det} - I_{BKGD}$	/	/	2D	No need of postprocessing	/	Dynamic biological imaging	[15]
STEDD	Multiple scanning Intensity subtraction	$I = I_{STED} - \alpha I_{solid}$ $I = I_{STED} - I_{hollow}$ $I = I_{STED1} - \alpha I_{STED2}$	2	$1/8\lambda$	2D,3D	Decreased uncorrelated background	Signal loss	Dynamic biological imaging	[16, 19, 35, 128, 132, 188]
SHRImP	Photobleaching of dyes	$I = I_{pre} - I_{post}$ $I = I_{a1} - I_{a2}$	/	$1/5\lambda$	2D	Advantageous in densely-packed dye region	CCD noise	High-density mapping of features	[142, 143]
NALMS	Photobleaching of dyes	$I_3 = I_{interval3} - I_2 - I_1$	/	$1/50\lambda$	2D	Ultrahigh resolution	CCD noise	DNA mapping	[144]
BaLM	Photobleaching of dyes	$I = I_{off} - I_{post}$ (or $I = I_{on} - I_{pre}$)	/	$1/8\lambda$	2D	No need of special dyes	Increased overall background	Multicolor mapping	[146]
PiMP	Photobleaching of dyes	$D_n(x,y) = \alpha_n I_n - I_{n+1}$	/	$1/5.5\lambda$	3D	Fewer images required	Slow timelapse imaging	Multicolor 3D imaging	[147]
eMSIM	Phase subtraction	$I_{diff} = I_{Gauss} - \alpha I_{Dnut}$	0.6	$1/5.6\lambda$	2D	Lower phototoxicity	Doubled acquisition time	Dynamic biological imaging	[153]
SPEM	Saturated absorption	$I_{sub} = I_{wf} - I_{SPEM}$	/	$1/8\lambda$	2D,3D	Cheap lasers	High risk of photobleaching	Semiconductors imaging	[150, 151]
FND-BS	Lifetime separation	$I = I_{long} - I_{short}$ $I_{lock\text{-}in} = I_{mw\_open} - I_{mw\_close}$ $I_{lock\text{-}in} = I_{mag\_close} - I_{mag\_open}$	/	/	2D	Decreased autofluorescence	/	Long-term in vivo imaging.	[41, 43, 44, 195–197]
NIRES	Saturated absorption Intensity subtraction	$I_{sub} = I_g - \alpha I_d$	/	$1/16\lambda$	3D	High reoslution	/	Deep tissue imaging	[36, 37]
MANP	Near-field detection	$I_{sub} = I_{conf} - I_{dCSD}$	/	$1/4.8\lambda$	2D	Easy implementation	Complexity in light path	Quantum sensing	[198]
DA-2P	Intensity subtraction	$I = I_{unaberrated} - I_{aberrated}$	/	/	3D	Low background	Unsuitable for sparse dye region	Deep tissue imaging	[59, 200]
2P-FED	Intensity subtraction	$I_f = I_g - \alpha I_d$	Wighted	$1/2.4\lambda$	2D	Enhanced spatial resolution	Signal loss	Biological samples	[73]

(*Continued*)

© 2020 Wiley-VCH GmbH

Table 1. Continued.

Imaging technique[a)]	Subtractive method	Equation[b)]	Optimal coefficient	Resolution[c)]	2D/3D	Advantage[d)]	Disadvantage[d)]	Application	Reference
SHG	Intensity subtraction	$I_{sub} = I_g - \alpha I_d$	0.5	$1/3.8\lambda$	2D	Resolution improvement	Signal loss	Biomedical research	[63, 158]
THG	Lock-in modulation	$I_{sub} = I_{w/o} - I_{\pi}$ $I_{sub} = I_{\pi} - I_{\pi/2}$	/	/	2D	No response at the wings	/	Quantum sensing	[158]
CARS-D	Vectorial beam Intensity subtraction	$I_{sub} = I_{on\_resonance} - I_{off\text{-}resonance}$ $I_{sub} = I_{peak} - I_{dip}$ $I_{sub} = I_{constructive} - I_{destructive}$ $I_{resonant} = I_1 - I_2 I_{1/2}$ $\Delta I_{as} = I_{as1} - k_M I_{as2}$	/	$1/2.7\lambda$	2D	Compatible to nonlinear imaging	Signal loss	Multimodal imaging	[60, 201, 208–210, 212-214]
DTA	Intensity subtraction	$I_{diff} = I_{solid} - I_{hollow}$	/	/	2D	Low laser intensity	Complexity in light path	Nanomaterial imaging	[227]
dSAX	Saturated absorption Photobleaching of dyes	$I_{sub} = I_{pre} - I_{post}$	/	$1/3.5\lambda$	2D,3D	Higher SNR	/	Turbid tissue imaging	[62, 183, 229, 230]
DIR	Intensity subtraction	$PSF_{DIR} = PSF_{gauss} - PSF_{vortex}$	/	$1/10\lambda$	2D	Resolution improvement	More noise-sensitive	Turbid tissue imaging	[61, 74, 216]

[a)] Full names are provided in Figure S1 of the Supporting Information [b)] Those equations are alternated slightly for format uniformity [c)] The data is obtained from original sources of the reciprocal references [d)] Only list the crucial advantages and disadvantages.

techniques, especially in nonlinear optical imaging (NLO). Finally, a summary and a general outlook are presented. We believe that this review will serve as a guide for better understanding the recent strategies that aim to improve optical super-resolution imaging (SRI) and will enlighten and inspire future work in super-resolution imaging utilized for the life science community.

2. Principles

2.1. SNR Improvement

There exist three types of noise: shot noise, read noise, and dark noise. Shot noise is the paramount and cannot be diminished based on hardware solution. Read noise is the signal uncertainty in the readout process when the detector transforms the light signals into electric signals. The dependency of SNR on the received photon number is shown in **Figure 1**b. In the case of ultralow received photons, especially when less than 100 photons, the influence of read noise increases drastically, resulting in a nonlinear relationship between the SNR and photon number. Besides, the thermal effect of silicon device will also lead to extra electrons resulting in dark current or dark noise. To this end, signal-to-noise ratio (SNR), as an important physical criterion that defines image quality, is presented by the Equation (1)

$$\mathrm{SNR} = \frac{s \times \eta}{\sqrt{n_s^2 + n_r^2 + n_d^2}} \quad (1)$$

where s denotes the signal, η stands for the quantum efficiency, n_s is the shot noise, n_r is the read noise, and n_d denotes the dark noise. For practical demand in experiments, SNR needs to be larger than 20:1 in order for quantitative measurement of the biological imaging. Whereas SNR > 5:1 is sufficient for useful information extraction from the background influence. In the case of high intensity illumination or long pixel dwell time with high photon number, SNR is mainly dominated by the square root of shot noise. It is noteworthy that the relative intensity noise, also known as $1/f$ noise, should be discussed especially in the signal modulation scheme of optical sub-diffracted microscopy (Figure 1c).[64]

Super-resolution microscopes extract higher resolution spatial information than would be possible in standard diffraction-limited systems (Figure 1a).[65,66] However, the resolution enhancement trades with useful signal decrease or required higher collection rate. In order to fulfill the Nyquist sampling criterion, the pixel size in an image should be at least 2-fold as fine as the desired resolution. Further, an N-fold increase in image resolution in D-dimensions requires an N^D-fold decrease in pixel size, i.e., a microscope which doubles resolution in 3D must therefore collect at least ≈8× as much signals in the same time as a conventional microscope for the same SNR. Thus, for pointwise scanning scheme, the super-resolved microscopes should collect N^{2D}-fold as much useful signals with no compromise of SNR. Otherwise, the collection rate must be increased by N^{2D}-fold without compromising imaging speed, due to the required reduction in pixel dwell time. Although the rigid requirement can be fulfilled by increasing the available probes density or by raising the

© 2020 Wiley-VCH GmbH

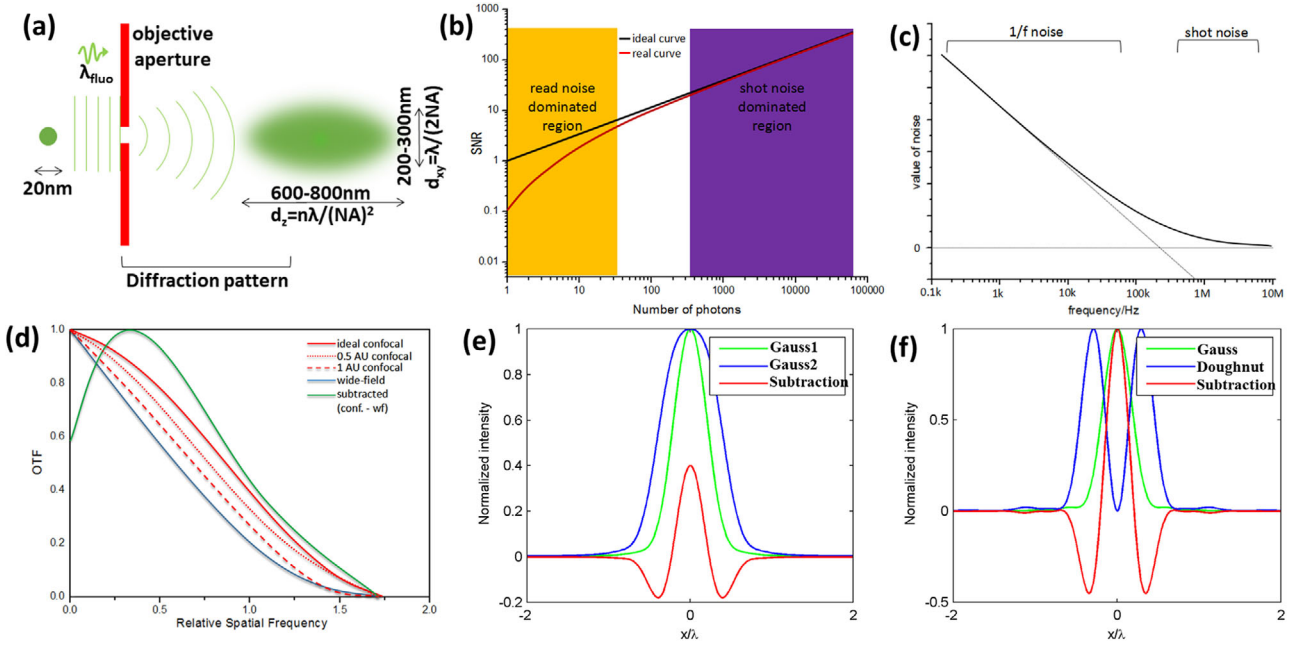

Figure 1. The schematic illustration on several concepts: spatial resolution, SNR, noise, and signal subtraction and so on. a) Schematic diagram of diffraction limit. In the diffraction limit criterion, d denotes resolution, λ is the imaging wavelength, n denotes the reflection index and NA stands for the numerical aperture. b) Relationship between SNR and photon number. c) Relationship between $1/f$ noise and modulation frequency. d) Optical transfer function (OTF) of confocal, widefield, and differential images. It is seen that high-frequency component increases in confocal microscopy with small pinhole sizes. Similarly, subtraction method enhances the high-frequency component. e) The subtraction between both Gaussian PSFs. f) The subtraction between doughnut-shaped and Gaussian PSF. DL: diffraction limit; conf: confocal; wf: widefield.

illumination power, factors, like sample fluctuation and photobleaching, make practical experiments even difficult to maintain the resulting SNR.

2.2. Resolution Enhancement

The subtracting method includes two steps: The optical imaging procedure and the digital processing. In the first step, two images are acquired under two different conditions, such as different phase masks, different amplitude masks, different polarization states, or different acquisition times. Subsequently, subtracting the two images is presented as shown in Equation (2)

$$I_{\text{sub}} = I_1 - \alpha I_2 \tag{2}$$

where I_1 and I_2 are the images acquired under different conditions and α is the subtraction coefficient.[67] The intensity values for images, I_1 and I_2, can be presented via the point spread function (PSF) h and the object o as following: $I = h \otimes o$. The intensity values of the image depend on the PSF h and the sample o. Thus, we can rewrite the equation based on PSF analysis as shown in Equation (3)

$$h_{\text{sub}} = h_1 - \alpha h_2 \tag{3}$$

where h_1 and h_2 are the PSFs of the images, respectively; h_{sub} is the differential PSF. There are two major types of PSF subtraction: i) solid PSF and solid PSF (Figure 1e);[28,68–70] ii) Solid PSF and hollow PSF (Figure 1f).[5,36,71] Solid PSF denotes Gauss-shaped PSF and hollow PSF equals to doughnut-shaped PSF. In the first type of subtraction, small subtraction coefficient leads to low peak intensity value of the differential PSF. While, in the second type that the doughnut PSF is subtracted from the Gaussian PSF, the resulting full width half maximum (FWHM) is smaller than the FWHM of the first.[28] It is worth noting that while the saturation or other nonlinear process is involved, the resolution enhancement becomes more conspicuous.

However, the above-mentioned scenario is limited by the presence of negative values in the case of excessive subtraction.[72] These negative values routinely lead to signal loss and image distortion in the final image. Studies have demonstrated that the optimum subtraction coefficient strictly depends on the imaging mode and the sample type.[67] It has been numerically demonstrated that the subtraction coefficient should be set at a value when the peak intensity value of the differential image is not less than 60% of its initial value. For most cases, the optimal value of the subtraction coefficient is ≈0.5–0.6 (as shown in Table 1).[67] To date, several literatures have specifically investigated the subtraction coefficient based on the evaluation of the differential image in the Fourier domain.[73,74] The evaluating function $C(\alpha)$ can be presented by

$$\mathrm{C}(\alpha) = \frac{\sum \left|\mathrm{FFT}(I_1 - \alpha I_2)\right| \sqrt{(u^2+v^2)/(u_{\max}^2+v_{\max}^2)}}{\sum \left|\mathrm{FFT}(I_1 - \alpha I_2)\right|} \tag{4}$$

where u and v denote the corresponding pixel sizes of the image; FFT stands for fast Fourier transform. The weight factor $\sqrt{(u^2+v^2)/(u_{\max}^2+v_{\max}^2)}$ increases linearly with the spatial

© 2020 Wiley-VCH GmbH

frequency so as to give a large weight to higher frequency components. Accordingly, the function $C(\alpha)$ displays a maximum for the optimal choice of α.[19] This method can be especially advantageous for nanoscopy on living cells or tissues, as the fluorescence decay time of a fluorophore can change due to interactions with the complex environment.

3. Methods for Improving SRI

3.1. Pinhole-Dependent Method

As is known, out-of-focus fluorescence routinely blurs the in-focus signals and quantitative analysis of 3D biological details is precluded in widefield microscopy. In CLSM, a pinhole is utilized to reject out-of-focus background signals which is therefore capable of optical sectioning.[3] Other approaches, like multiphoton microscopy and light-sheet microscopy, also possess the ability to extract focal plane signals. In order to further increase the resolution of CLSM, subtracting the images acquired by pinholes with different sizes can increase the system resolution with only minor modification in the detection component.[75] The sizes of the two pinholes are usually determined as follows: The small pinhole is nearly the size of the diffraction limited Airy-disk while the large pinhole has a size corresponding to approximately the second dark ring of the Airy-disk.[28] Figure 1d shows the rationale in resolution enhancement through subtraction from the frequency domain. The PSF FWHM of the resulting image could be enhanced up to half of that of conventional confocal microscopy. It has been shown that for confocal fluorescence with a finite sized pinhole, the optical transfer function (OTF) can actually go negative, so that subtraction can actually increase signal for particular bands of spatial frequencies.[76] In previous report, the subtraction of images acquired by using different wavelengths has also been investigated.[68] Because the widefield illumination could be recognized as an infinitely-sized pinhole that contains a large amount of out-of-focus information, the optics resolution could be enhanced while the widefield image is subtracted from the confocal image.[28] Moreover, the annular, D-shaped or fan-shaped pupil filter scheme is also a feasible approach for improving the axial resolution of the optical microscope.[77] Note that the as-mentioned method will lead to the useful signal decrease in condition of inappropriate differential.[28,70] According to Equation (3), an optimal value of the subtraction coefficient should be carefully selected to achieve a tradeoff between the resolution and image quality. In practical experiments, intensity matching, prior knowledge, and the specific area of the sample have to be considered when determining the optimal value.[67] For detailed study on the pinhole-dependent subtraction method, readers can refer to the published reports.[28]

To emphasize, the methodology of increasing the system resolution and improving image SNR can be utilized to the widefield case, with pinholes substituted by phase masks. In order to extend the depth of field (DOF) in a hybrid imaging system, symmetrical and asymmetrical phase masks are applied and the two widefield biological images are therefore subtracted.[78,79] In our perspective, the subtraction of the different backfocal plane intensities can be used to reconstruct unknown wavefronts without the reference wave.[80] Apart from far-field modalities, phase-mask-based subtraction also works well in a near-field setup (**Figure 2**b).[81] Superoscillation microscopy, a kind of near-field microscopy technique, is a phenomenon where the local oscillation of a wave is faster than the largest global Fourier frequency of the wave. Optical superoscillation microscopy can achieve high resolution and large depth of field.[82] However, a major drawback is the inevitable presence of high-energy regions away from the superoscillation region, which leads to a tradeoff between the duration and the effective bandwidth of the superoscillation region. By subtracting the modulated image (using a vortex phase mask) from the unmodulated superoscillation image, sidebands could be eliminated (Figure 2c). Total internal reflection fluorescence microscopy (TIRF) is another classical near-field imaging technique and the resolution could be further enhanced based on stochastic photobleaching subtraction algorithm.[83]

3.2. Photon Reassignment

In order to further increase the attainable resolution of classical confocal microscopy, photon reassignment technique, such as image scanning microscopy (ISM) and detector array microscopy (DA),[84–88] has been proposed. The only minor modification for the confocal optical system is to replace the pinhole with a charge-coupled device (CCD) or the detector array at the pinhole plane. Theoretically, another 1.4-fold resolution enhancement can be facilitated compared with confocal microscopy. In DA microscopy, like Airyscan[89] or virtual *k*-space modulation optical microscopy (VIKMOM),[90] a detector array is able to collect signals at the peripheral regions of the Ariy-disk and can solve the pile-up effect caused by the dead time of electronics.[91] The resolution-improved confocal microscope based on array detection and photon reassignment has been extended to commercial application in biomedical research and clinical diagnosis.

The detector array is composed of various detectors instead of a single point-detector such that the location offset of each detector causes a distinct effective PSF.[92] The combination of the images captured by the peripheral detectors results in the creation of an image with a doughnut-like effective PSF, while the combination of center detectors results in a sharper solid effective PSF. Therefore, the subtraction of the two reconstructed images will elicit a sharper PSF and higher spatial frequency (Figure 2a).[91] Moreover, subtraction of the original signals obtained by the detectors in the outer ring from the reassigned signals could similarly increase the final spatial resolution. In addition, according to previous reports, shrinking the pinhole size will further sharpen the size of the overall 3D PSF. The subtraction process could also cause the axial response to be sharper, thereby increasing the high-frequency weight in the axial direction.[93] After photon reassignment, more high-frequency information can be obtained to enhance the spatial resolution and SNR. Every detector contributes a small portion of imaging information and thereby, the spatial resolution and SNR are balanced. To date, ISM and DA microscopy have been gradually applied to quantum imaging and biological imaging in brainstem, cells and microtubule networks.[6,88,94]

© 2020 Wiley-VCH GmbH

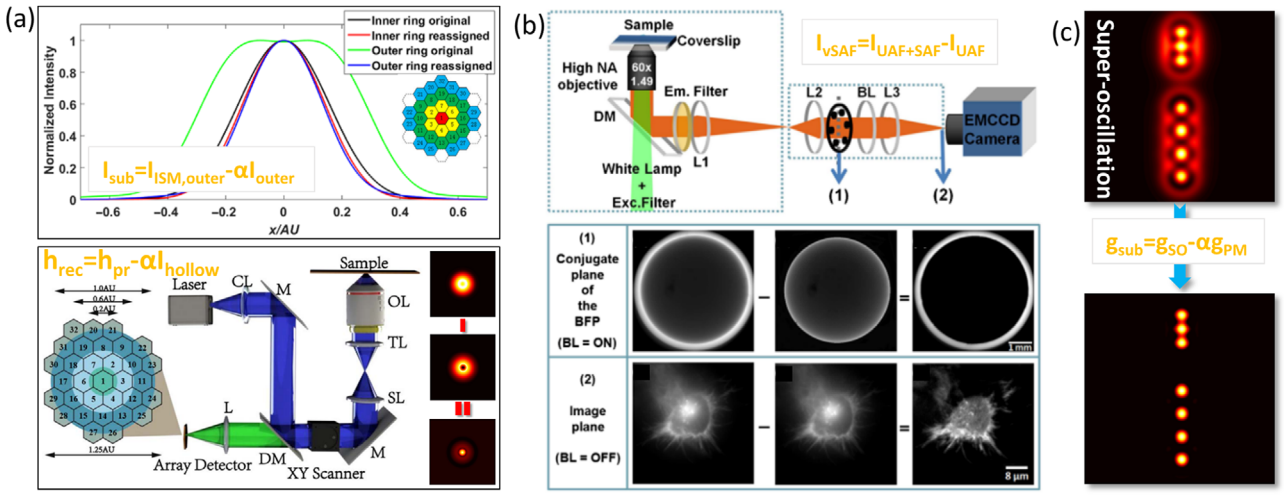

Figure 2. a) Photon reassignment technique. Top: subtraction of signals obtained by original outer ring detectors from pixel reassigned signals of outer ring detectors.[91] Bottom: subtraction of the image acquired by doughnut beam from the image by Gaussian beam via detector array imaging.[93] b) Virtual supercritical angle fluorescence microscopy (vSAF). Top: the optical system of vSAF; Bottom: the working principle of vSAF. Reproduced with permission.[81] Copyright 2012, American Physical Society. c) Suppression principle of side-lobes in superoscillation microscopy by the phase mask modulation. Reproduced with permission.[231] Copyright 2018, Elsevier B.V.

3.3. Switching Laser Mode Differential Method

Recently, some cost-effective and easily implemented solutions have been introduced in the visualization of tissue structures and sub-cellular dynamics, such as structured subtraction microscopy (SSM),[95] fluorescence emission difference microscopy (FED)[5] and switching laser mode microscopy (SLAM).[96] Shown in **Figure 3**a,b, these techniques are based on the intensity difference between two images acquired by switching laser modes: bright mode (like Gaussian illumination) and dark mode (like azimuthally polarization or 0–2π phase modulation). To date, resolution as high as sub-50 nm, 1/20th of the excitation wavelength, has been achieved in imaging of inorganic nanoparticles through turbid biological tissues.[36] This is a flexible approach for either nonfluorescent modality or classic fluorescence imaging system.[97] Currently, this technique is conjugated with extensive imaging techniques, such as STED,[98] multiphoton excitation (MPE),[36] light-sheet fluorescence microscopy (LSFM) and so on (Figure 3f).[99] Extensive theoretical and experimental researches have investigated the advantages and characteristics of this differential method.[67,100–104] However, due to the mismatching of bright mode and dark mode, signal loss tends to occur in case of excessive subtraction, leading to image deformation of cells or tissues.[72] Extensive efforts have focused on PSF engineering in order to decrease the negative values.

3.3.1. PSF Matching

Take fluorescence emission difference microscopy (FED) as illustration, in order that Gaussian PSF and doughnut PSF are modulated to achieve the best match, a diaphragm is added to the excitation light-path so that the rays at the margin area of the entrance pupil are blocked and the solid focal spot could therefore be extended.[71,102] Cylindrical vector beams, like radial polarization (RP) beam and azimuthal polarization (AP) beam or higher-order azimuthal polarization (HAP) beam, are superior to conventional Gaussian illumination in ameliorating the image distortion.[105,106] By virtue of the combination of RP and AP beams with specific parameter, solid beam with flat-top profile PSF is generated. Because the intensity profiles of the HAP beam (squeezed hollow spot) and the flat-top beam (extended solid focal spot) are almost identical, subtracting the two could facilitate deformation-free imaging which is advantageous in observation of microtubule details (Figure 3c).[107] This strategy may be applicable to 3D molecular orientation analysis by combining the transverse electric field produced by different beam.[101] In our perspective, the criteria of extending the solid spot and shrinking the hollow spot for accommodating PSF profiles is believed to hold great potentials to facilitate deformation-free imaging in cell biology and medical therapy in the future.[72]

3.3.2. Saturated Excitation

Using a saturated solid excitation spot, a flattened and extended solid focal spot is obtained.[92,108] Meanwhile, using a saturated doughnut excitation spot, a center-shrunken doughnut focal spot is obtained. Given the nonlinear effect caused by the saturation of the fluorescence emission at high illumination intensity, both the solid and hollow focal spots contain high spatial frequency components. The center-shrunken doughnut focal spot indirectly improves the resolving ability with a notable performance. Previous literatures have experimentally demonstrated that the negative intensity values in the differential image are reduced.[108] Also, saturation excitation is flexible to other techniques, like detector array imaging. However, high intensity excitation and nonlinear absorption leads to severe photodamage of the living samples. Adoption of nonbleaching labels, such as upconversion nanoparticles (UCNPs), is expected to address this problem.[36,37]

© 2020 Wiley-VCH GmbH

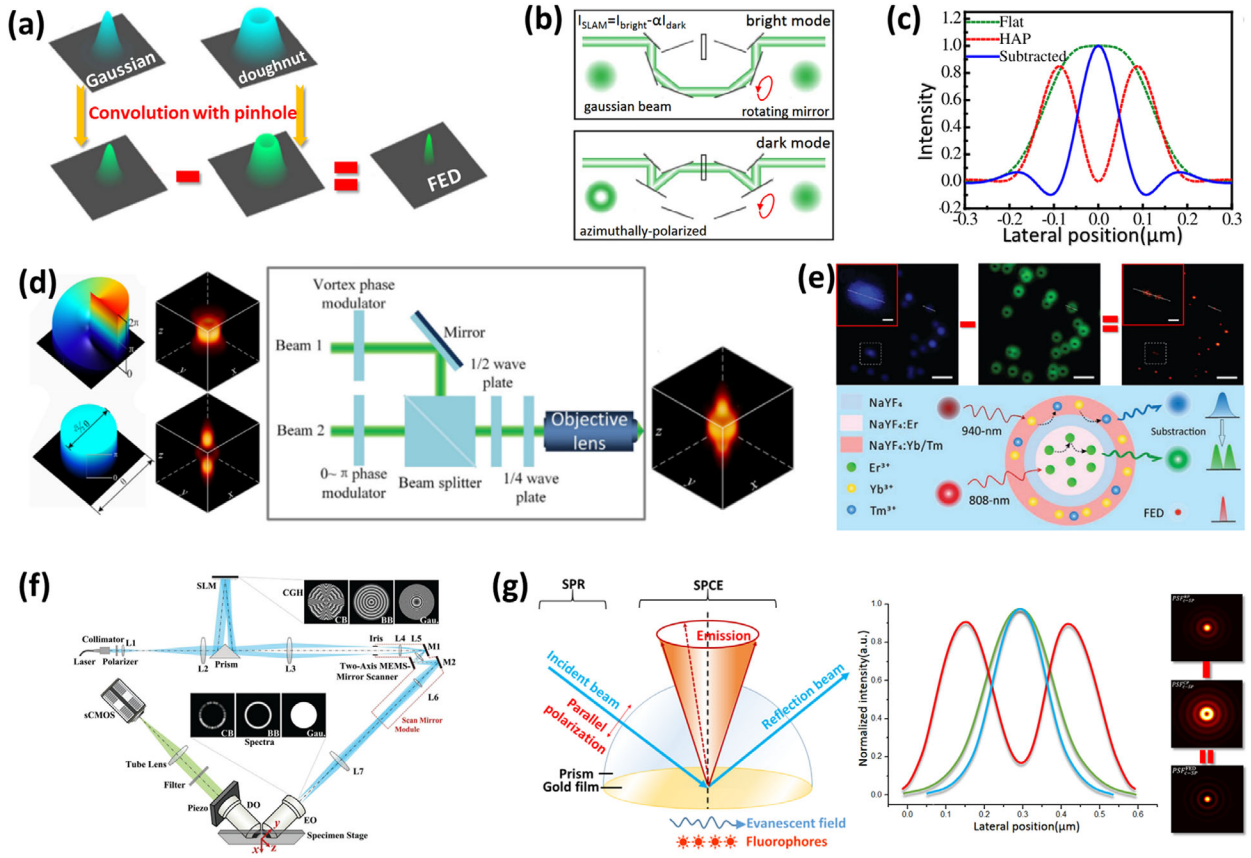

Figure 3. a) The working principle of fluorescence emission microscopy (FED).[5] b) The rationale of switching laser mode microscopy (SLAM). Reproduced under the terms of an open access license.[96] Copyright 2013, Optical Society of America. c) PSF matching of flat-top beam and higher-order radial polarization (HAP) beam in order to reduce negative values in subtraction process. Reproduced with permission.[101] Copyright 2014, Optical Society of America. d) Compact system of 3D FED. With 0–2π phase plate, laser beam is modulated in lateral direction into hollow profile while axial direction using 0/π phase plate. The two modulated beams are combined into 3D hollow spot. e) Working principle of one-scan FED. Top row: image subtraction of the long-wavelength from the short-wavelength. The two insert images are reciprocal magnified details. Scale bar in three images: 1 μm; scale bar in the magnified two images: 200 nm. Bottom row: energy absorption and fluorescence emission of upconversion nanoparticles (UCNPs) in one-scan FED. Reproduced with permission.[163] Copyright 2018, Royal Society of Chemistry. f) Complementary beam subtraction (CBS) microscopy. Reproduced with permission.[99] Copyright 2018, John Wiley and Sons. g) Left: rationale of surface plasmon-coupled emission (SPCE) microscopy.[113] Right: subtracting the images with and without vortex phase plate (VPP), respectively, in order to enhance the attainable resolution in SPCE.[71] SPR: surface plasmon resonance.

3.3.3. Adaptive Subtraction Coefficient

For switching laser mode differential method, two images are consequently taken with Gaussian and doughnut-shaped excitation beams, and afterward the two images are subtracted from each other with an appropriately normalized coefficient. Unfortunately, the shortcoming is the data loss caused by direct subtraction of normalized data sets. Manual selection of the most appropriate subtraction coefficient is not only time consuming, but also is unsuitable for samples with densely-packed structure distribution. A weighted subtracting coefficient value algorithm for universal utilization will be highly desirable so that not only image contrast and resolution can be enhanced, but over-subtraction and image deformation are also avoided. The key novelty of the proposed approach lies in pixel-by-pixel assessment with respect to the intensity difference between initial images. Also, the similar adaptive methodology can be applied to better matching of the two PSFs at their periphery, involved with the identification of a kernel matrix that minimizes the error function.[74] The approach involves the identification of a suitable linear operation of the Gaussian image pixels that are optimized to achieve a subtracted PSF that is narrowed with little or no side-lobes.

3.4. Surface Plasmon-Coupled Emission Microscopy

Due to the features of noninvasive and high sensitive detection, fluorescence imaging is widely utilized in extensive fields, such as microscopic bioimaging, biomedical medicine research, and in vivo diagnosis. However, it remains challenging for monitoring and analyzing cellular and biomolecular dynamics in nanoscale and detecting extremely small molecular events in subcellular environments where ultrahigh sensitivity is especially required.[109] Surface plasmon-coupled emission microscopy (SPCE) is an effective technique that exploits the advantage of surface plasmon resonance (SPR) to intensify the

© 2020 Wiley-VCH GmbH

fluorescence adjacent to the surface of a metal film coated on glass slides.[71,110–112] The coupling between fluorophores and surface plasmon polaritons (SPPs) is beneficial for increasing the SNR and minimizing photobleaching due to the directional fluorescence emission at the surface plasmon resonant (SPR) angle. The schematic working principle is shown in Figure 3g.[113]

3.4.1. Plasmon-Assisted Techniques

Currently, in order to achieve high contrast recording, SPEC has become the crucial connection point in biological observation, linking super-resolution imaging techniques (like STED,[114] SMLM, SIM[115–117]) with nonlinear optical imaging techniques (like CARS, SHG).[118,119] Numerical studies show that Rayleigh scattering by 80 nm gold nanospheres is about 5 orders of magnitude higher than fluorescence emission by the traditional fluorophores. This feature could allow for higher localization precision.[117] For example, fluorescent emitters are attached to subdiffracted plasmonic nanoparticles and by single molecular localization-based method the reconstructed image could reveal the hidden structure of the nanoparticles. However, unlike general SMLM, within each diffraction-limited spot, two different emission sources should be accounted for: the stochastic fluorescence from the fluorescent probes and the steady background luminescence of the metal nanostructures (like gold nanorods). To isolate the fluorescence counterpart, the average gold nanorod luminescence contribution is subtracted.[116] In a similar manner, the plasmon resonance of metal nanoparticles can be used to strengthen the stimulated depletion effect of excited molecules with 50% resolution enhancement compared to fluorescent-only probes.[114] In this plasmon-assisted STED method, subdiffraction imaging of adult neural stem cells is obtained at lower depletion powers with diminished unwanted background light. Alternately, surface plasmon could form interference patterns for illumination with much higher spatial frequencies, based on the fact that SPPs have larger wave vectors than free space light.[117] To this end, plasmonic SIM is feasible to further increase the spatial resolution compared with conventional SIM by elaborately engineering the plasmonic structures, like using plasmonic nanoparticle arrays.[115] In our perspective, STED microscopy is seen possible to combine with SIM by SPR enhancement to facilitate resolution increase and phototoxicity decrease in the study of the basal membrane of live cells.[120]

Also, SPEC holds great promise to conjugate with inorganic materials, like QDs,[121] UCNPs,[122] FNDs, and fluorescent polymer,[110,123] to achieve versatile functional imaging. For instance, in order to obtain the SPP propagation distance, subtracting the confocal fluorescence images which are measured after and before photobleaching, respectively, produces the field distribution signature of the surface plasmon. This strategy is implemented in a thin film of fluorescent polymer coated on top of gold nanowires.[110] Alternately, subtracting the radiative decay rate and the surface plasmon generation rate from the total decay rate obtained through the lifetime analysis, the exciton decay rate to nonradiative damping channel is extracted.[121] For this end, the exciton-plasmon coupling process in a coupled system composed of a single QD and a silver nanowire could be analyzed. In addition, by subtractive method, plasmon-assisted TIRF can accomplish functions, like higher spatial resolution and larger imaging depth with high contrast. SPCE presents thriving vigor in conjugation with TIRF.[109] Detailed investigations are provided in the published literatures.[124,125]

3.4.2. Differential SPCE

In practice, SPCE is inherently limited by its optical characteristics in the process of signal detection. For example, biological ambient, like a cell, is an inherently scattering matrix which is challenging for high contrast recording.[126] To overcome this, a dual-wavelength technique (one resonant and the other nonresonant) is employed to investigate mixtures of plasmon nanostructures (e.g., gold nanoparticles) and cell lysate. Because cell lysate presents wavelength-insensitive scattering, such that when two images of cell lysate acquired with different illumination wavelengths are subtracted, a flat background could be observed. Meanwhile, because the gold nanoparticles present wavelength-dependent plasmon resonance, a strong nanoparticle scattering remnant remains after subtraction.

Alternately, because of the highly directional polarization of the fluorescence in SPCE microscopy, the fluorescence PSF is modulated into an undesirable doughnut shape which is unfavorable for imaging.[127] In order to address the issue, the fluorescence detection is divided into two light paths that one light path is modulated by a 0–2π vortex phase plate (VPP) while the other remains unchanged.[71] Subtracting the two detection windows will effectively increase the final resolution. Nonetheless, image distortion occurs simultaneously, resulting in either positive side-lobes or negative side-lobes. Adding a diaphragm could alleviate this problem. It is worth noticing that axial positioning will introduce changeable transverse PSF shapes from a solid spot to a hollow spot within one wavelength in the vicinity of the focal plane. To take advantage of this characteristics, subtraction of off-focus frame from on-focus frame can achieve resolution improvement in SPCE.[111] In this strategy, negative values are greatly suppressed. We should emphasize that radially polarized (RP) incident light will lead to solid transverse PSF while circularly-polarized (CP) light results in a hollow PSF. Subtraction of fluorescence signals that are excited by RP incident light and circularly polarized (CP) light, respectively, can sharpen the resulting transverse PSF (Figure 3g).[112] The enhancement of this configuration in the resolution is 33% compared with conventional SPCE microscopy. To conclude, the growing partnership between super-resolution imaging and plasmonics has presented in various ways that the two topics mutually benefit one another to extend our understanding of the nanoscale world.

3.5. Stimulated Emission Depletion Microscopy

Stimulated emission depletion microscopy (STED), as one of the paramount super-resolution techniques, has been widely utilized in the biological and physical community. According to the resolution formula $d = \lambda/(2\mathrm{NA}\sqrt{1 + I_{\max}/I_0})$, where d is the resolution for STED, λ is the excitation wavelength, NA is the numerical aperture, $I_{\max}$ is the depletion intensity, and I_0 is the threshold intensity, in order to achieve ideal imaging result, $I_{\max}$ must be

© 2020 Wiley-VCH GmbH

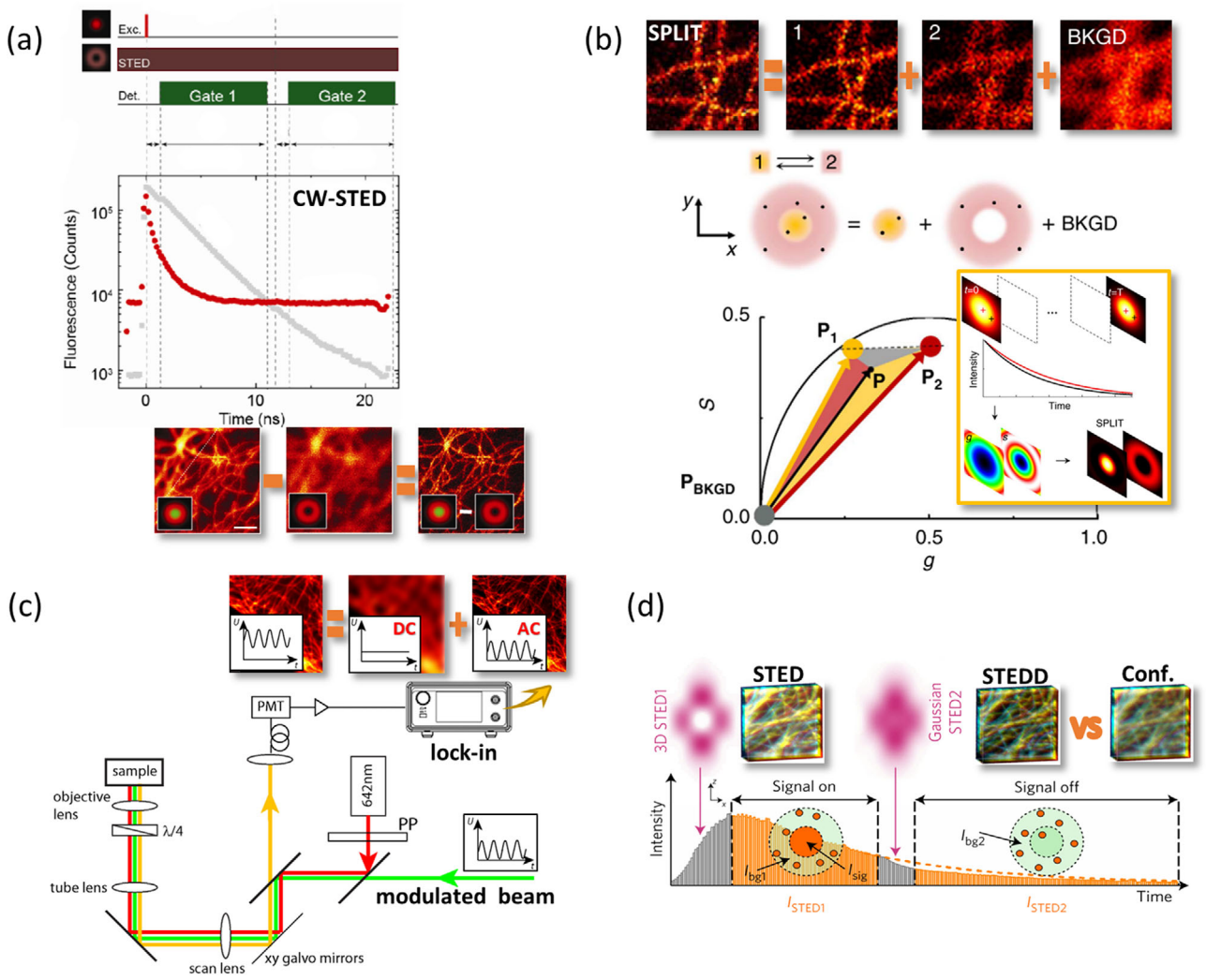

Figure 4. Graphic schemes of background suppression techniques in STED nanoscopy. a) Subtractive time-gating strategy in removing AStEx background. Reproduced with permission.[14] Copyright 2012, Optical Society of America. b) The strategy of temporal tuning for removing the AStEx background. *P1* and *P2* denote two separate temporal components of the resulting temporal vector *P*. Reproduced with permission.[17] Copyright 2015, Springer Nature. c) Signal modulation in order for background-free imaging. Reproduced with permission.[15] Copyright 2013, Optical Society of America. d) The scheme of stimulated emission double depletion microscopy (STEDD). The SNR of the acquired image is greatly enhanced compared with conventional STED nanoscopy. Reproduced with permission.[132] Copyright 2017, Springer Nature. BKGD: background; PMT: photo multiplier tube; PP: phase plate.

much (routinely several orders of magnitude) higher than I_0. Under ultrahigh depletion radiation, severe background signals are generated by secondary excitation of the depletion illumination. This background signals mainly arise from anti-Stokes excitation (AStEx) which has so far prohibited STED microscopy from reaching its theoretically molecular resolution.[14] Also, broad halos around the bright spots re-excited by the depletion beam and incompletely depleted fluorescence could be simultaneously observed in conventional STED images.[128] Indeed, unique to 3D imaging of biological samples, the incompletely depleted fluorescence background is derived from the off-focus incomplete quenching. To date, various background suppression techniques are developed to inhibit the three kinds of background: i) AStEx; ii) incompletely depleted fluorescence; iii) the incompletely depleted fluorescence.

3.5.1. Subtractive Time-Gating

Subtractive time-gating is an easily-implemented way to reduce the AStEx background in STED microscopy.[129] Two time windows are involved: i) The open window where the excitation beam and depletion beam are applied so that central useful data and unwanted background signals that are evoked by the depletion beam are both collected. ii) The close window where only the depletion beam is applied so that merely background signals could be collected (**Figure 4**a).[18,130] The subtraction of the close window from the open window will reject the background data. Considering the pulsed excitation beam and continuous wave (CW) depletion beam as illustration, Gate 1 is used for detection at the time window ranging from 0.5 to 4.5 ns while Gate 2 is used for time window ranging from 4.5 to 8.5 ns. Since the lifetime of the

© 2020 Wiley-VCH GmbH

fluorescent dyes is routinely ≈3 ns, Gate 2 range includes only signals emitted by the depletion beam. Indeed, the signal subtraction of Gate 2 from Gate 1 will result in the decrease of background signals. The gating method with subtraction is especially promising for depletion beam wavelength closer to the emission maximum, even at the emission maximum.[14] The effectiveness is verified by the improved image quality of microtubules in Hela cells. However, over blue-shifted wavelength may also lead to severe photobleaching. Therefore, there should weight the balance of the wavelength selection, photobleaching, and undesired background signals. Moreover, in the case of low received photon counts, the ending range of the fluorescence signals is non-negligible. Ignorance of this ending range will yield underestimated background signals.[130] In either CW-STED or pulsed STED configuration, utilization of a field-programmable gate array (FPGA) is advantageous in background suppression in which an open time window and a close time window are involved in every pixel unit.[18]

3.5.2. Temporal Tuning

To the best of our knowledge, at each pixel a given number of photons N are detected stemmed from an undetermined number of fluorophores at unknown positions within the diffraction-limited (DL) volume. One way to reduce this indetermination is to reduce the fluorescent molecule number into one (the stochastic switching scheme, like SMLM), or by restricting the possible positions of fluorophores within the DL volume (the targeted switching scheme, like STED). For this end, super-resolved resolution can be obtained with a method that encodes information from the saturated spatial channels of the microscope system into the temporal channel and decodes it after the transmission. An early confocal-based implementation has been realized to decode the spatial information based on the fact that the spatial distribution of the illumination intensity induces a spatial-dependent temporal dynamics. The methodology could be applied to suppress the background signals. By generating spatially controlled gradients in the fluorescence lifetime, an approach, called separation of photons by lifetime tuning microscopy (SPLIT), enables nanometer-scale imaging of microtubule structures (Figure 4b).[17] The excitation region is split into two concentric areas. Due to the radial symmetry of the STED doughnut spot, the fluorescence from each area shows a unique dynamic corresponding to the local average STED beam intensity. With phasor analysis on the TCSPC histogram of photon arrival time, a decomposition is employed to extract the signal only from the central subregion. Notably, the phasor analysis succeeds in distinguishing the dynamic component of the central region not only from that of its neighborhood, but also from the anti-Stokes background which is uncorrelated with the excitation laser cycle and thus lies at the origin in the phasor domain. Note that exploiting more dynamic components helps to achieve higher resolution, but is practically limited by shot noise which compromises accuracy. Alternately, it is well-known that a high intensity of quenching light will shorten the lifetime of the fluorophores in the illuminated region by stimulated emission effect. The lifetime discrepancy caused by different intensity radiations can be utilized to extract highly resolved spatial information. With specific subtraction coefficient, subtraction of the images with short and long lifetime gating could facilitate resolution enhancement. The method can differentiate between features of dimensions of $\approx\lambda/7$.[34]

3.5.3. Signal Modulation

The molecular imaging of thick biological tissues (normally the multiple-scattering medium) suffers from scattering background. Focal modulation technique is therefore developed for suppressing the background fluorescence signal excited by scattered light which is validated in fluorescence images of chondrocytes. Using a spatial phase modulator in the excitation light path, the intensity of fluorescence signals derived from the focal volume only is modulated even when the focal spot is located deep inside a turbid medium. The oscillatory component in the detected fluorescence signal can be readily differentiated from background signal caused by multiple scattering. This strategy allows simultaneous acquisition of confocal (unmodulated) and modulated images. The methodology can also be applied in background suppression of AStEx signals in STED microscopy. Using a lock-in amplifier and an optical modulator, such as an acousto-optic modulator, the excitation light path could be temporally modulated while the depletion light path remains unmodulated so that the fluorescence re-excited by quenching radiation becomes uncorrelated background (Figure 4c).[15] This approach is quite straightforward and results in the removal of undesired excited signals. Indeed, the method is more flexible in the choice of the excitation and depletion wavelengths, and is expedient in lowering the power density of the depletion beam. Additionally, a priori knowledge of the living specimens is not needed. The process can be accomplished in real time compared with other time-consuming subtractive postprocess solutions. Using well-suited lock-in instrument with even wider bandwidth and ultrahigh shot-noise limited sensitivity can further increase the acquisition speed. In addition, the costly modulation hardware can also be replaced by other cost-effective solutions in low-frequency range, like electronic frequency band pass or a fast Fourier transform (FFT) strategy.[15,131]

3.5.4. Multibeam Scanning

Subtraction of the image obtained in a confocal scanning setup from the image obtained in a STED setup is expected to further increase the system resolution compared with the conventional STED by multibeam scanning.[35] Also, multibeam scanning is an effective way to fight against the uncorrelated background signals. Because of the characteristic spectrum of quantum dots (QDs), STED imaging in QD-labeled structures suffers from the dim halo, the re-excited background caused by depletion radiation. The image acquired with illumination by the depletion beam only is subtracted from the STED image to achieve background-free imaging.

The off-focus incomplete depletion background, another kind of background in common STED imaging, is difficult

© 2020 Wiley-VCH GmbH

to identify, because it can only be detected in the presence of the excitation beam. A method called stimulated emission double depletion microscopy (STEDD) aiming at suppressing the AStEx signals and incompletely depleted background simultaneously, particularly in 3D-STED setups.[16,132] In STEDD, specially, another Gauss-shaped pulse (STED2) is added to a normal STED setup, resulting in the depletion of fluorescence from the central subregion of the excitation volume. Therefore, the remaining photons after the STED2 pulse in the TCSPC recording are merely from the excitation by the depletion pulse and off-focus incomplete depletion that is escaping from the STED2 pulse. A proper scaling of the remnant fluorescence is subtracted from the time-gated STED image so that the background could be sufficiently suppressed (Figure 4d).[132] Nonetheless, STEDD is found to be with hardware complexity since three pulses should be strictly controlled in temporal domain.

Another easily implemented technique, called polarization switching (psSTED), could achieve background-free STED imaging through a straightforward subtraction of the recorded background from the regular STED image.[133] The background is acquired by switching between two different circularly polarized states of the depletion beam. The experiment and simulation works have demonstrated that direct re-excitation background is mostly due to high STED power while the incomplete depletion background is mostly due to low STED power. Indeed, this technique is limited because polarization switching is dependent on a time-consuming motorized rotation stage at the risk of light path instability. In the future, electro-optic equipment is expected to further ameliorate the optical system.[134] Note that *Z*-STED spot is much more susceptive to aberration and refraction index mismatch compared with *XY*-STED. By updating the vortex phase pattern with a bi-vortex pattern on the spatial light modulator (SLM), the final coherently superposed doughnut spot produces stronger depletion in the defocused region and therefore reduces off-focus background.[135] Another technique, utilized in STED nanoscopy using hyperspectral detection arrangement, is to unmix signals from four fluorescence markers.[128] This method could achieve four-color recording using only two lasers. Double scanning is also needed and the STED-only scanning frame must be subtracted.

To sum up, current researches on alleviating the background noise problem in STED have been presented, which is particularly critical when imaging dense samples. Variants, like subtractive time-gating, temporal tuning, signal modulation, and multibeam scanning, are effective for addressing unwanted background signals problem in common STED setup, each of which has its own unique application regime. For example, subtractive time-gating is especially useful to diminish the early insufficiently excited fluorescence. While, multibeam scanning is particular suitable for simultaneous suppression of uncorrelated background caused by depletion beam and off-focus incompletely depleted excitation fluorescence background in 3D STED configuration. Besides the techniques mentioned above based on hardware and light paths, various computational methods were also intensively utilized for improving the STED image quality against background noise, like rolling-ball background subtraction.[32,136–138]

3.6. Single Molecule Localization Microscopy

In SMLM, a sparse subset of fluorophores is activated at each single illumination and then the reconstructed image is obtained by stacking tens of thousands of frames.[9] The label density limits the resolution due to the Nyquist criterion: The separation between neighboring localizations must be one half of the desired resolution.[139] In living cell measurement, the temporal resolution is thus ultimately limited by the switching kinetics of the fluorophore, the camera frame rate and the field-of-view, in order to satisfy the Nyquist criterion for a given spatial resolution. In addition, all SMLM strategies suffer from the problematic bleaching of organic dyes which reduces the observation time and degrades the image quality. The recently presented technique, called MINFLUX, could achieve molecular localization with far less photons, greatly ameliorating the photobleaching effect.[140,141]

Interestingly, the seemingly harmful bleaching characteristics of fluorescent dyes can be utilized to achieve a high spatial resolution. One strategy, called single-molecule high-resolution imaging with photobleaching (SHRImP) initially entails the localization of the two fluorescent dyes.[142,143] SHRImP acquires the first image (I_{pre}) and subsequently bleaches one of the fluorescent dyes and localize the other to obtain a second image (I_{post}). The subtraction of I_{post} from I_{pre} can recover the intensity distribution of the bleached dyes (**Figure 5**a1,2). This method is easily-implemented and only requires one type of fluorescent label, which can also be extended to multiple-dye modality. In nanometer-localized multiple single-molecule technique (NALMS), up to 20 fluorescent molecules can be separated.[144] NALMS has the potential to be conjugated with other super-resolution techniques, such as points accumulation for imaging in nanoscale topography (PAINT).[145] However, the distance of two dyes should be well separated and this method is limited to a 2D condition. In addition, low noise CCDs with high quantum efficiency are also required. It should be noted that the above-mentioned methods cannot be used in densely packed fluorophore region.

Based on the blinking/bleaching properties of fluorophores, off/on event can be detectable via subtraction method and the image series can be utilized to reconstruct super-resolved images in highly density regions of features (Figure 5b1,2).[146] A method called bleaching/blinking assisted localization microscopy (BaLM) does not require bleaching prior to the detection of the fluorescent dyes as in the case of PALM or STORM. Note that the overall background signals are increased because subtraction treatment combines the background data of two images. This disadvantage may be compromised by background suppression using lock-in detection in the future. Another stochastic-bleaching-based method, called PiMP (subtraction of measured value from estimated decay images), explores the positions at which the bleaching molecule deviates from the expected (average) bleaching per frame (Figure 5c1,2).[147] Compared with PALM method, fewer images are required for the reconstruction using PiMP because more information per differential image is utilized. However, artifact regions between structures could be generated as a result of the simultaneous and uniform bleaching of two adjacent structures. In a nutshell, the above-mentioned bleaching-based approaches combined with subtractive dealing are versatile and advantageous for super-resolution

© 2020 Wiley-VCH GmbH

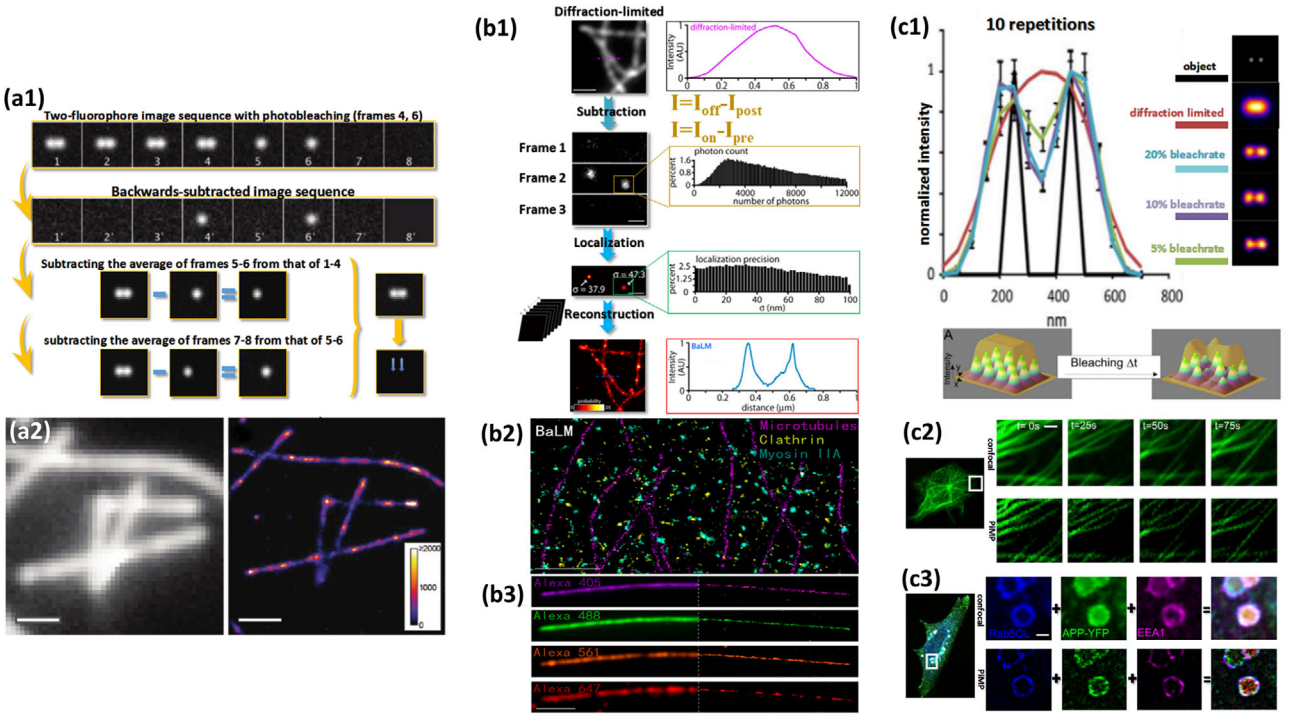

Figure 5. Resolution enhancement and SNR improvement in SMLM. a1) Working principle of generalized single molecule high-resolution imaging with photobleaching (gSHRImP); a2) Left: diffraction limited image; Right: super-resolved image using gSHRImP. Reproduced with permission.[143] Copyright 2011, American Chemical Society. b1) Rationale of bleaching/blinking assisted localization microscopy (BaLM). b2) Imaging result using BaLM. b3) Left: diffraction limited image; right: highly resolved image using BaLM. Reproduced with permission.[146] Copyright 2011, National Academy of Sciences, U.S.A. c1) Schematic diagram of photobleaching microscopy with nonlinear processing (PiMP). c2) Left: the mouse embryonic fibroblast cell. Top right: time-lapse confocal images highlighted with the white square in the left image. Bottom right: the reciprocal super-resolution PiMP images. c3) Left: the Hela cell transfected with different kinds of labels. Top right: the confocal images. Bottom right: the PiMP images. Reproduced with permission.[147] Copyright 2012, Company of Biologists Ltd. Scale bars in (a2), (b1) top, (c2), (c3): 1 μm; Scale bar in (b1) middle: 0.6 μm; scale bars in (b2) and (b3): 2 μm.

imaging (SRI) due to their simple configuration and ultrahigh spatial resolution. Note that over subtraction should be avoided which yields increased noise and a reduction in SNR, thereby decreasing the localization accuracy.

3.7. Structured Illumination Microscopy

SIM and its many variants are useful tools in the nanoscopic study of biological systems, realizing relatively high spatial resolution and video-rate recording.[148] SIM can be used for optical sectioning and the rejection of background signals. However, the sectioning ability of SIM becomes increasingly challenging in case of the thick samples which are scattering mediums (>20 μm).[149] Out-of-focus background adds to this challenge. Several methods have been proposed to overcome this problem. In nonlinear SIM or saturated patterned excitation microscopy (SPEM),[150,151] subtraction of a suitably scaled SPEM image from a widefield image would decrease the background noise. In multifocus SIM (MSIM), the optical sectioning advantage of confocal microscopy is conjugated with the resolution-doubling characteristics of SIM (**Figure 6**a,b).[152] The 2D excitation patterns are generated by a digital micromirror device (DMD), allowing for rejection of out-of-focus light. The distance of the spaced foci should be cautiously selected. Nonetheless, the best absolute resolution achieved by MSIM is slightly lower than that of the existing 3D SIM because the multifocal excitation patterns contain all spatial frequencies permitted by the objective. Using a 0–2π phase shift and adding another beam illumination, subtraction of the Gaussian beam image from the doughnut beam image can further increase the MSIM spatial resolution.[153] However, this is at the price of lengthening acquisition time.

In order to further decrease the scattering influence in depth, as well as the out-of-focus signals, multiphoton excitation combined with MSIM possesses the ability to reject out-of-focus background by replacing the DMD with a microlens array which is efficient in high light transmission.[154] In regard to reducing the acquisition time of 3D SIM, a two-step processing method has been proposed: First, the out-of-focus background is removed; Secondly, the two-beam harmonic illumination pattern is utilized.[155] Presently, extensive applications have shown the powerful imaging capability of subtractive SIM in biological studies. For example, a strategy called multiangle interference microscopy (MAIM) combines TIRF-SIM and multiangle evanescent light illumination to achieve depth imaging with high SNR and relatively high temporal resolution in subcellular structures (microtubules, mitochondria, peroxisomes).[148] MAIM aims to break the axial diffraction limit

© 2020 Wiley-VCH GmbH

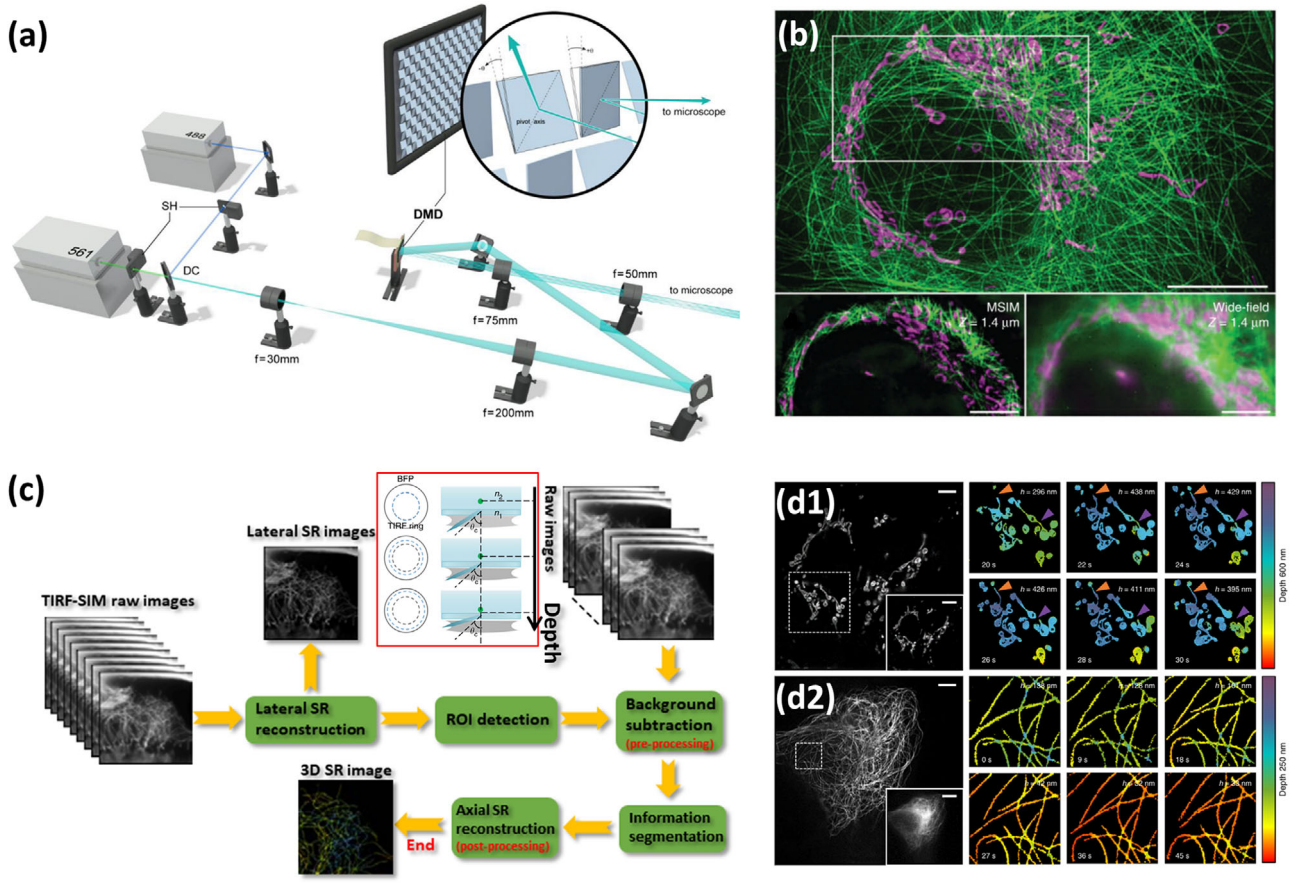

Figure 6. Resolution enhancement and SNR improvement in structured illumination microscopy (SIM). a) Optical setup of multifocal SIM (MSIM). b) Imaging result of MSIM, displaying the microtubules (green) and mitochondria (magenta) in a fixed U2OS cell. Bottom left and bottom right are slices boxed in upper part by MSIM and widefield microscopy, respectively. Reproduced with permission.[152] Copyright 2012, Springer Nature. c) Workflow of multiangle interference microscopy (MAIM). Noise and background in the image stacks may lead to incorrect depth information and confuse the true sample information, which need to be subtracted in the preprocessing. The insert red box denotes the multiangle illumination for depth-imaging. d1) Left: lateral super-resolution image of mitochondria in the U2OS cell. Right: the time-lapse 3D volume super-resolution images of the ROI (white dashed line box in the left). d2) Left: lateral super-resolution image of microtubules in the U2OS cell. Right: the time-lapse 3D volume super-resolution images of the ROI (white dashed line box in the left). Reproduced with permission.[148] Copyright 2018, Springer Nature. Scale bar in (b): 5 μm; Scale bar in (d1), (d2): 10 μm. MA: multiangle; BFP: back focal plane; ROI: region of interest.

to facilitate imaging with high axial resolution. Nonetheless, noise and background occur during acquisition of stacks of images which would add incorrect axial or depth influence to original 3D biological structure. In the reconstruction algorithm, the noise and the background need to be subtracted beforehand (Figure 6c,d1,2).

3.8. Faster for Biological Application

In order to achieve real time imaging in vivo, high speed acquisition or high temporal resolution is particularly expected for biological application in optical super-resolution microscopy. To date, speed limitations exists due to inherent optical design in spite of increasing developments in hardware and more photostable, brighter fluorescent markers that facilitate more sensitive and faster acquisition. For example, in pointwise scanning scheme, by replacing the nanopositioning stage with a galvo mirror, the pixel dwell time could be shrunken to 2 from 200 μs,[156] boosting the acquisition speed to one frame per second (fps). The above-mentioned light-weight mirror enables ≈kHz scan rates over large of field which is particularly suitable for neuronal activity study and can also be substituted by an acousto-optic or electro-optic modulator for even faster scanning concern. Other routes include spinning disk, temporal focusing, light-sheet microscopy which have proved especially useful in neurobiology.[157,158] As it is known, applied with multiple excitation foci to illuminate the specimens, parallelization illumination can achieve high speed imaging while widefield microscopy exemplifies the highest degree of parallelization.[159] However, in parallelization system, signal crosstalk from neighboring pixels largely spoils the in-focus recording.

The four factors—hardware, light path, algorithm, probes—influence each other and should be interlinked in order for best image quality during super-resolution recording.[159] For

© 2020 Wiley-VCH GmbH

instance, the instinct spectral selection of excitation and depletion beams determines specific fluorophores that are needed in STED microscopy. Imaging in case of unsuitable probes is often quite noisy due to re-excitation of depletion radiation.[160] Instead, before multiemitter fitting algorithms are invented, permitting greater numbers of molecules to be localized in any given frame, SMLM is inherently limited by the number of molecules that may be switched on and localized at once. Currently, the fastest method of super-resolution microscopy is linear structured illumination microscopy (SIM) that can be used with conventional (nonswitchable) fluorophores. However, SIM works with the need for sophisticated and expensive electronics.

In a similar manner, for FED or SLAM super-resolution microscopy, it requires double scanning to obtain one frame, which is the inherent hardware limitation that slows down the acquisition speed and increases the risk of sample drifting. Using a detector array device, only one scan of the doughnut-shaped beam is needed. The difference between the reconstructed image by photon reassignment (hollow PSF) and the image recorded by the center detector (solid PSF) can be utilized to decouple the spatial structure information of the microtubule samples. The proposed strategy, based on photon reassignment, is insensitive to noise compared with deconvolution algorithm or Fourier filters.[161] In another variant, subtraction of the image by hollow spot array from the widefield image could can speed up the image acquisition compared with conventional FED.[162] Recently, a related research has exploited the advantage of upconversion nanoparticles (UCNPs) to overcome the aforementioned problem (Figure 3e).[163] The as-prepared UCNPs, with special design and control, can be excited by two lasers, respectively, to emit two different wavelengths simultaneously with little crosstalk. After collecting the two fluorescence signals, subtraction of the two imaging results will reduce the acquisition time.

3.9. Axial Resolution Enhancement

Optical microscopy permits 3D investigation of living cells, tissues, and even small organisms. However, in practice, because of complex biological ambient in cells and tissues, it is normally difficult to extract axial information for quantitative analysis. To date, extensive methods have been developed for delineating the structures and functions of the tissue samples. For example, two-photon adaptive optics microscopy is applied in the deep tissue imaging, mostly in the brain tissue for neurobiology research.[164,165] Light sheet microscopy has been widely used in high-throughput imaging, like whole-brain imaging in *Drosophila*.[157] The abovementioned 3D imaging techniques nonetheless remain axially diffraction-limited.

The axial super-resolved technique is extremely important for providing improved tomographic or optical sectioning ability and is favorable for examining not only relatively thin samples such as the plasma membranes, but also thick samples such as mammalian cells.[166] The common rationale is to shorten the axial extent of the point spread function (PSF). The emergence of 3D sub-diffractive imaging, like 4Pi-STED,[167] 3D-RESOLFT,[168] 3D-STORM,[169] biplane FPALM, and 3D-SIM,[170–172] particularly works with circumventing the axial diffraction barrier in visualization of subcellular structures. Optical hardware configuration is attached great importance in those techniques, like two opposing objectives, annular phase plate, cylindrical lens, the beam splitter, and EMCCD camera. Other variants rely on beam phase modulation induced by a spatial light modulation (SLM) in order to accurately determine axial position of the fluorescent probes, generating PSFs like double-helix PSF and self-bending PSF.[173,174] Unlike STED or SIM that requires complicated optics, 3D quantum dot blinking imaging is generally more convenient and commercial quantum dots with various emission spectra are readily available.[175,176] By subtracting the adjacent frames, the common background is subtracted off. However, it is worth-noting that due to frame-subtracting, no motion from frame to frame should be required. Similarly, the subtraction modality can be applied to confocal-based optics, using only one SLM to modulate the excitation beam laterally and axially into a 3D hollow profile (Figure 3d).[177] Subtracting the axially-modulated frame from the Gaussian axial frame facilitates axial resolution enhancement. Improper subtraction caused by sample drifting can be avoided utilizing the one-scan technique (Figure 3e).[178,179] This technique holds potential in the axial and depth visualization of organisms, like zebrafish.[180] Factors, like hardware, probes, algorithm, interact with each other and play an important role in enhancing the axial the resolution and reducing the background noise.

3.10. Inorganic Nanoparticles

Nowadays, inorganic nanoparticles are attracting increasingly attention and are widely used in biological and physical researches, because of their excellent features including photostability, biocompatibility, flexibility, and so on. Inorganic nanoparticles, like quantum dots (QDs), upconversion nanoparticles (UCNPs), and fluorescent nanodiamonds (FNDs), show nonbleaching performance in bioimaging which is superior to organic compounds.[181,182] The nonbleaching characteristics can greatly suppress the negative impact of photobleaching during long-term recording so that high contrast and sustainable acquisition could be realized. Combined with these inorganic probes, modulation in optical systems could facilitate impressive capabilities in super-resolution microscopy, such as background suppression,[16] dual-color imaging,[183] ultrahigh resolution imaging, and so on.[36]

3.10.1. Quantum Dots

Quantum dots are single colloidal semiconductor crystals, routinely a few nanometers in each dimension, whose size and shape can be precisely controlled by the duration, temperature, and ligand molecules. By chemical synthesis, QDs could have composition- and size-dependent absorption and emission.[184] The unique optical properties of QDs make them appealing as in vivo and in vitro fluorophores in a myriad of

© 2020 Wiley-VCH GmbH

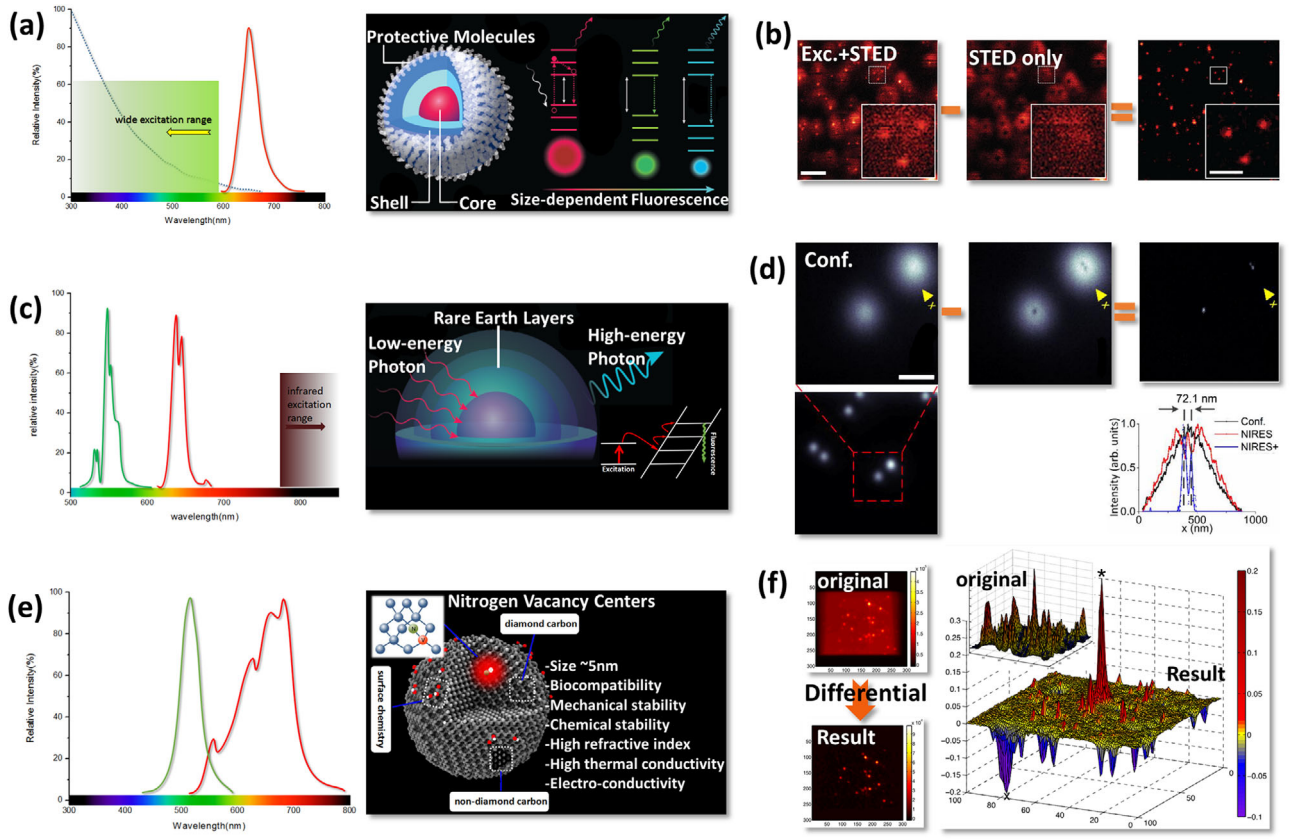

Figure 7. The characteristics, advances and applications of three kinds of inorganic nanoparticles: QDs, UCNPs, and FNDs. a,c,e) The absorption and emission spectra, atomic structure and energy level. a) Reproduced with permissions.[181] Copyright 2016, Springer Nature. e) Reproduced with permissions.[182] Copyright 2018, Springer Nature. c) Reproduced with permissions.[232] Copyright 2017, Elsevier. b) Double scanning scheme in STED marked with QDs in order to eliminate the background caused by secondary excitation stemmed from depletion beam. Reproduced with permission.[16] Copyright 2015, Springer Nature. d) Subtraction of images acquired by confocal and hollow beam scanning, respectively, in multiphoton near-infrared saturated (NIRES) imaging conjugated with UCNPs. Bottom right is the PSF comparison of confocal image and NIRES image. Reproduced with permission.[36] Copyright 2018, Springer Nature. f) Application of FNDs in background suppression of super-resolution imaging. Upper left and bottom left are the original image and the resulting image, respectively. Reproduced with permission.[41] Copyright 2013, Optical Society of America. Right part is the 3D data of the fluorescence intensity. Scale bar in (a): 0.3 μm; Scale bar in (d): 0.5μm.

biological investigations, in which conventional organic fluorescent labels fall short of providing long-term stability and simultaneous detection of multiple signals.[185] For example, because QDs feature a broad excitation spectrum and a narrow emission spectrum, multicolor imaging becomes available with only single wavelength laser source in super-resolution microscopy.[176]

To date, only a few reports have described the successful application of QDs in STED due to some limitations. On the one hand, auger recombination is known to prevent efficient stimulated emission of isolated QDs. By synthesizing QDs with an exceptionally thick shell, stimulated emission and excited-state absorption mechanisms could work either independently or synergistically to realize the quenching. A 7-fold improvement over the diffraction barrier was generated.[186,187] Nonetheless, the extended size of the QDs seriously hampers their biological application. On the other hand, QDs have characteristically broad excitation spectrum that reaches deeply into the emission band which makes it difficult to identify a wavelength at which optical de-excitation by stimulated emission or a similar transition prevails (**Figure 7**a).[16] This problem can be overcome using background suppression technique. The aforementioned multibeam scanning is an effective way to reduce the unwanted background contribution in imaging of ZnS-coated or $CsPbBr_3$ QDs.[188] In order to eliminate the dim halo that is present after the process of excitation followed by depletion, a second hollow depletion beam is utilized and two images are recorded by the two scans. Subtracting the two images could erase the uncorrelated background (Figure 7b).[16] Nonetheless, this is time-consuming due to double scanning to acquire one frame. For the above-mentioned approaches, all exploit an incoherent fluorescence response to the lasers. Nanoscale imaging of molecules is possible by exploiting the intensity-dependent molecular switch. Recently, a scheme that relies on a coherent response to a laser is developed based on an ensemble of quantum dots by quantum control of a two-level system via rapid adiabatic passage. Emitter position determination with a factor of 10 is obtained.[189] QDs are believed to hold great potential utilized in super-resolution microscopy and further studies are expected in the near future.

© 2020 Wiley-VCH GmbH

3.10.2. Upconversion Nanoparticles

Upconversion nanoparticles (UCNPs) have attracted significant interests as powerful and useful biolabels for optical imaging and super-resolution microscopy because they show characteristics of non-photobleaching and non-photoblinking under continuous laser illumination.[36,37] In addition, the novel materials have narrow absorption and emission bands, and their compositions (like sensitizers and activators) and structures (like core and core–shell) can be easily controlled to obtain the intended spectral properties (Figure 7c).[163] Because UCNPs could upconvert near-infrared photons into visible and ultraviolet ones, a low saturation intensity of ≈0.19 MW cm^{-2} in STED microscopy is recorded with an ultrahigh resolution in imaging single 13 nm UCNPs and cellular cytoskeleton protein structures are visualized with relatively high acquisition speed.[190] The large anti-Stokes spectral separation between excitation and emission renders the probes highly useful in background-free and photostable bioimaging.[191] In addition, UCNPs are particularly suitable for fluorescent emission difference microscopy. Related research result shows that during 30 min radiation, the fluorescence from UCNPs exhibits no attenuation, presenting high resistance to photobleaching.[37] Recently, deep tissue super-resolution imaging has been achieved using multiphoton excitation and subtraction technique and deconvolution algorithm in the near infrared regime (Figure 7d).[36]

3.10.3. Fluorescent Nanodiamonds

Fluorescent nanodiamonds (FNDs) are biocompatible for in vivo imaging.[192] Recently, they have been shown to be useful for orientation measurement in fluorescent markers.[193] The negative-charged nitrogen-vacancy (NV^-) centers are responsible for the fluorescence emission (Figure 7e). As is known, biological samples tend to generate autofluorescence that contaminates the image quality. NV^- centers have lifetime of ≈20 ns, far longer than the lifetime of the autofluorescence (1–4 ns).[192] This discrepancy can be exploited to separate the two signals in the temporal domain so that the autofluorescence can be effectively eliminated by time-gating.[194,195] Additionally, based on the optic-magnetic property of FNDs, the microwave radiation at 2.87 GHz will lead to spin transition from $m_s = 0$ to $m_s = \pm 1$ (Figure 7f). Subtracting the image acquired without microwave radiation from the image with microwave radiation will result in improved image contrast and background-free data (Refer to Table 1 for the equation). Nonetheless, frame-by-frame subtraction will increase the risk of image drift and the request for the system stability. Furthermore, the lock-in modulation method is not only suitable for physical imaging processes, but also for biological detection. Based on the electron spin characteristics of FNDs, when a magnetic field is applied, the sublevels $m_s = \pm 1$ will split into $m_s = +1$ and $m_s = -1$ and a change in the fluorescence intensity of FNDs occurs (Figure 7f).[41,44,196] This specific interaction is exclusive to FNDs rather than the surrounding autofluorescence. Using lock-in detection scheme, the useful, wanted signals can be extracted, and the unwanted background can be filtered when the magnetic modulation is employed to the living samples. Note that the subtraction method is also expedient in probing individual electronic spin in diamond, using RESOLFT.[197] In another variant, with the array of near-field probes, the relationship between the NV center ensemble and a metal nanostructure is explored.[198] Subtraction of the readout signals from the confocal signals yields resolution improvement. With an increase in the light intensity of the doughnut-shaped laser beam, the final resolution could be further increased.

4. Nonlinear Optical Imaging

Nonlinear optical imaging (NLO) is a novel and important imaging method and can facilitate quantitative analysis of structures or features ranging from organelles (sub-100 nm) to the entire cells (≈10 µm). The nonlinear optical imaging family consists of several imaging techniques: two-photon excitation (2PE), three-photon excitation (3PE), second harmonic generation (SHG), third harmonic generation (THG), coherent anti-Stokes Raman scattering (CARS), infrared imaging absorption (IRA), pump–probe microscopy and so on.[58] The energy level systems are shown in **Figure 8**a1–e1, respectively.[199] However, each NLO modality has its own limitation. Current nonlinear optical imaging variants call for further optimization to accommodate complex biological observation. For example, 2PE microscopy is suitable for deep tissue imaging due to its high optical sectioning ability. However, the spatially confined focal spot of 2PE is at the price of a high excitation power which may cancel out the optical sectioning benefit.[59] Subtraction technique can be used to remove the background inference caused by thick sample scattering and at the same time the required laser intensity could be decreased.[200] Alternately, subtraction technique is also useful for the nonresonant background in CARS.[201] A detailed discussion on NLO is presented elsewhere.[199] Subtraction method also have the potential to facilitate the achievement of higher resolution and improved SNR in other newly rising imaging techniques, such as quantitative phase imaging (QPI),[202] quantitative mass imaging (QMI),[57] photoacoustic microscopy, and so on.[51,52] This section focuses on the combination of subtraction technique with NLO imaging and includes a detailed discussion concerning biological applications.

4.1. Multiphoton Excitation

Unlike single-photon excitation (SPE), two-photon excitation (2PE), or three-photon excitation (3PE) performs optical sectioning in scanning microscopy, generating little out-of-focus fluorescence, i.e., out-of-focus photobleaching is largely suppressed.[9] Additionally, deep penetration is achieved in biological tissues due to the use of longer wavelengths such as in the near-infrared (NIR) region, which are beneficial for minimization of photodamage. However, 2PE or 3PE is generated by ballistic or unscattered light and the proportion of unscattered light decays exponentially within the focal depth.[200] Increasing the laser power may compensate for the depth limitation, otherwise out-of-focus background signals are generated, especially in the case of dense labeling. In order to reduce the background noise and to increase the imaging rate, temporal focusing of the excitation pulse is applied instead of spatial focusing.[203] The laser

© 2020 Wiley-VCH GmbH

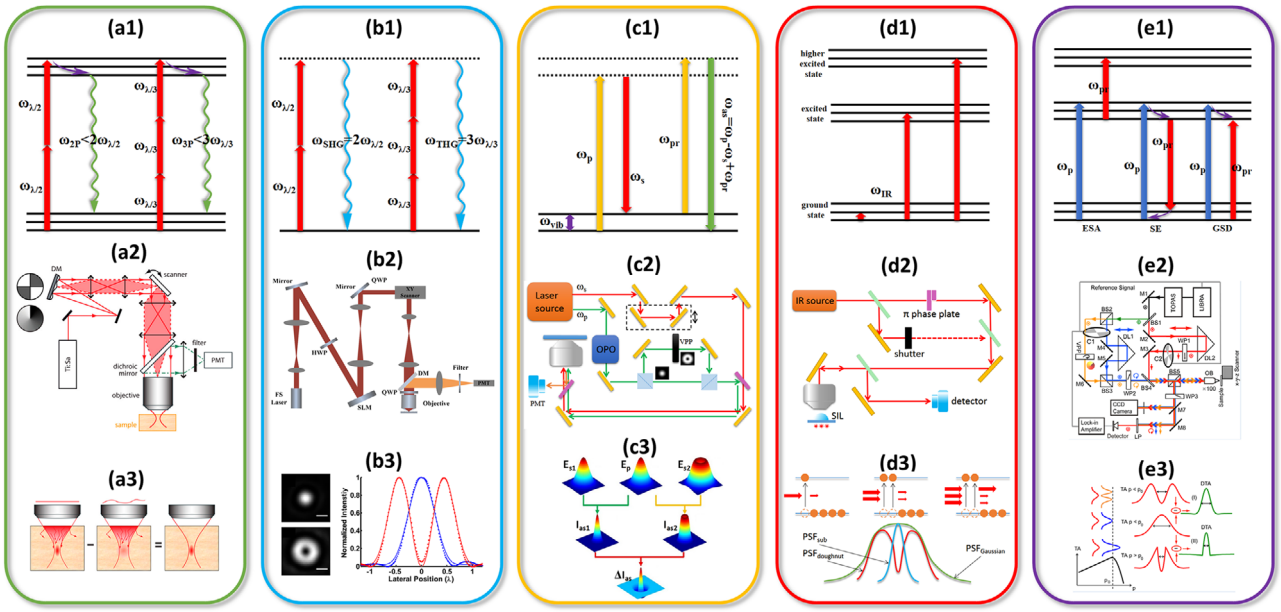

Figure 8. Overview of nonlinear optical imaging (NLO) and the variants for improving nonlinear optical imaging (NLO). a1–e1) energy-level schemes of 2PE (3PE), SHG (THG), CARS, IRA imaging, pump–probe microscopy, respectively. a2–e2) Optical setups of DA-2P, differential SHG, CARS-D, differential IRA imaging, and DTA, respectively.[59,63,74,215,227] a3) Subtraction of the images with and without aberration will decrease the background noise in 2PE. Reproduced with permission.[59] Copyright 2008, Elsevier. b3) Subtraction of the images acquired by solid and hollow beams greatly increases the resulting resolution. Reproduced with permission.[63] Copyright 2015, Springer Nature. c3) Subtracting the images obtained by solid and hollow beams will increase the CARS image resolution.[60] d3) Gaussian and doughnut images are firstly filtered by the intensity weighted algorithm so that the two are better matched in PSFs. Subsequent subtraction of doughnut image from the Gaussian image will eliminate the side-lobes in infrared microscopy. e3) Subtraction of doughnut TA image from the Gaussian TA image will lower the intensity requirement and enhance the resulting image resolution. Scale bar in (b3): 500 nm. ESA, excitation state absorption; SE, stimulated emission; GSD, ground state depletion. Reproduced with permission.[227] Copyright 2016, American Chemical Society.

pulse traverses through each sample slice, achieves its shortest duration at the focal plane and stretches out again as it propagates beyond this region. Temporal focusing can be achieved by controlling the profile of the laser pulses. Therefore, the background noise can be subtracted from each image and corrected according to the spatial intensity of the Gaussian beam profile.

Another approach called differential aberration 2PE (DA-2P) involves positioning a digital mirror device (DMD) in the back aperture of the objective. The corresponding architecture is shown in Figure 8a2 and the subtraction rationale is shown in Figure 8a3 accordingly.[59,200] Unlike most adaptive optics strategies that attempt to improve the image quality in the focal plane, this method degrades the in-focus quality. Due to the nonlinear properties of 2PE and the fact that aberrations quench largely in the focal region, subtracting the image without DMD degradation from the image with the degradation will improve the image quality and reject the background interference (refer to Table 1 for the equation). It is worth noting that this method is most compatible with densely distributed dye regions. Indeed, although the penetration depth is increased, this approach is limited by imaging speed because two images must be taken sequentially. Alternately, a new strategy for two-photon differential aberration, based on near-instantaneous temporal multiplexing, is developed, enabling high-speed imaging with pixel rates.[39] Recently, saturated excitation was additionally introduced into a hybrid approach involving the subtraction method and 2PE, such that resulting images with sharper PSF and lower negative values could be achieved.[73] By virtue of saturated effect, a profile-extended solid spot and a center-shrunken hollow spot are generated. Using the same coefficient for the entire image can induce side effects, like side lobes and signal loss. Thus, the subtraction coefficient should be intensity-dependent and adaptively selected instead of a constant value.

4.2. Second (Third) Harmonic Generation

SHG and THG microscopy have been widely used in the characterization of biological samples and in the field of material science, based on nonlinear optical effect.[204,205] Considering SHG, it is based on the second-order coherent process, in which two low energy photons are upconverted to exactly twice the incident frequency, i.e., half the wavelength of the excitation radiance. As is well-known, two-photon excitation (2PE) is a two-photon process, and there is a loss of energy during the relaxation of the excited state. However, SHG microscopy is energy conserving. SHG is sensitive to non-centrosymmetric structures, and is viable for the imaging of biological structures such as microtubules, myosin, muscle, collagen, and so on.[204,206]

Higher resolution is demanded in the imaging of SHG and THG in order to characterize the fine structures or features in cells and tissues. Using a sharper focal spot may help to enhance the resolution, yet this will induce side lobes and degradation in

© 2020 Wiley-VCH GmbH

the axial image quality.[63] Similar to the aforementioned temporal focusing strategy to enhance axial resolution, a variant can be applied to the subtraction of the image with phase at π from that with phase at zero, or the subtraction of the image with phase at $\pi/2$ from that with phase at π (refer to Table 1 for equations).[158] 15% axial resolution improvement has been demonstrated. An alternative is to make a subtraction between two images scanned by a solid focal spot and a hollow focal spot, respectively (Figure 8b2,b3).[63] Compared with conventional SHG microscopy, this subtractive method is highly effective for achieving the resolution enhancement in the imaging biological tissues, such as the rat tail tendon and mouse leg muscle myofibrils. Although the signal field of SHG excitation which is a second-order nonlinear process is directly proportional to the conjugated product of the excitation field, the SHG intensity is dependent on the angle between the polarization direction of the excitation field and the molecular orientation. Thus, apart from the intensity distributions, additional polarization distributions in the focal field have to be considered, which rather adds to the complexity of the configuration.

4.3. Coherent Anti-Stokes Raman Scattering

Nowadays, CARS is a useful tool for noninvasive imaging of lipids and myelin, either in vivo or in vitro.[58,207] In the Raman spectroscopy architecture, a single wavelength beam is required to drive the electron oscillator and to obtain the characteristic frequency ω_v which denotes a unique molecular structure. In CARS, the characteristic frequency is not driven by a single optical wave but rather by the frequency difference between the pump beam ω_p and the Stokes beam ω_s. In other words, the laser beams at frequency difference $\omega_p - \omega_s$ establish the state coupling between the ground state and the virtual state, which represents the superposition of states in quantum mechanism, i.e., the molecule is in the ground state and the virtual state simultaneously. This state coupling could be probed using a third laser beam at the frequency ω_{pr}, which drives the molecule up to the virtual state. Note that the molecule will return back to the ground state, emitting anti-Stokes signals at the frequency $(\omega_{pr} + \omega_p - \omega_s)$. No energy conversion is involved in the CARS process.[208]

Nonetheless, one major limitation of CARS is the existence of a nonresonant background that is coherently mixed with the resonant signal of the features of interest.[209] Several variants of the technique have been proposed to address this problem including coherent anti-Stokes Raman scattering difference microscopy (CARS-D).[60] Digital subtraction of the off-resonance image from the on-resonance image can suppress the nonresonant background (refer to Table 1 for equations).[210] Note that this simple scheme is most advantageous for strong scatterers when the resonant contribution is much larger than the nonresonant background. This digital image processing technique only deals with the nonresonant signal during the process of image acquisition rather than during the generation or detection process. Alternatively, due to the line shape of spectral features in CARS, the resonance peak can be accounted for as the maximum and the resonance dip as the minimum and the backgrounds of the maximum and the minimum could be used for subtraction (refer to Table 1 for the equation).[211–213] Subsequently, the resulting images could be corrected according to maximum–minimum ratio of prerecorded CARS intensity distribution. This approach renders advantageous vibrational contrast for weak scatterers while the resonant component is insignificant compared with the nonresonant component.

Using the pulse shaping technique and the quantum coherent control method, the relative intensity of resonant contribution can be either maximized or minimized. Using lock-in detection, with subtraction of the two signals, the background-suppressed image could be achieved. Such a method can also be potentially applied to other nonlinear process, like 2PE and SHG.[208] Three pulsed lasers have also been used to improve the SNR and to reduce noise in digital subtraction with high-frequency repetition rates.[214] Among the resulting CARS signals, the resonant component and the nonresonant electronic background, only the first item is frequency-dependent. Under high-frequency modulation, the resonant useful component can be demodulated using lock-in amplifiers with the background noise filtered.[201] However, this frequency-modulated CARS (FM-CARS) modality is only suitable for the condition of low concentration. In analogy to FM-CARS, using dual pumps, a subtraction of two CARS results in a specific ratio and background influence could be greatly reduced.[209] Another optional scheme is particularly suitable for the condition when the resonant signals are larger than or comparable to the nonresonant background, which can be completely removed from the resulting image. The scheme is implemented by acquiring three images of the same sample region when the beat frequency on the optimal frequency is positive off half of Raman linewidth and negative off half of Raman linewidth, respectively. By subtraction of the two off-resonance images from the on-resonance image, respectively, the background could be highly suppressed (refer to Table 1 for the equation). Also, it is noted that the triple-frequency scheme is much more prominent for strong Raman scatterers than for the week scatterers. Moreover, the subtraction technique is also useful for enhancing the spatial resolution of CARS. An alternative approach has been proposed which involves with a pair of solid and hollow pump beams for improving the spatial resolution of CARS resonant (Figure 8c2,3). Vibrational anti-Stokes signals are obtained using a Gaussian mode and doughnut mode, respectively. Based on the subtraction of the latter from the former, significant resolution enhancement could be achieved.[60,215]

4.4. Infrared Absorption Imaging

Infrared absorption (IRA) imaging is a promising analytical strategy for biological structures within subcellular resolution and tends to provide complementary information in contrast to Raman Effect. It is a method that reveals the molecular fingerprints since the molecular vibrational modes are dependent on the chemical bonds in a material sample.[61,74,216] Nonetheless, the diffraction limit imposes a severe resolution ceiling for imaging detailed features. In terms of mid-infrared wavelengths, normally in 2–20 μm range, in order to circumvent the diffraction limit, several variants have been presented such as reflective objectives, crossed polarizations, and central solid immersion lens.[217,218] However, the resolution enhancements

© 2020 Wiley-VCH GmbH

of those endeavors are still limited. Numerical works have demonstrated the potential of subtraction method for enhancing resolution in the mid-infrared range. The mid-infrared central solid-immersion lens (c-SIL) microscopy exploits the subtraction method of a Gaussian beam with a c-SIL PSF and a second beam modulated using 0–π phase plate with a centrally hollow PSF (refer to Table 1 for the equation).[217] Thus, the solid Gaussian image is filtered using an intensity weighted matrix so that matches the hollow beam profile (Figure 8d2,d3).

4.5. Pump–Probe Microscopy

Pump–probe microscopy is a newly-rising and powerful technique in characterizing molecular specificity and dynamics.[64,219,220] There are three kinds of pump–probe modality: stimulated emission (SE), excited state absorption (ESA), and ground state depletion (GSD).[221–224] The transient absorption microscopy (TA), one type of ESA pump–probe microscopy, is utilized to obtain spatial information by virtue of saturated effect.[225,226] However, the saturation effect requires for high power density which is in high risk of ablating materials. An approach, called differential transient absorption microscopy (DTA),[227] is proposed exploiting the change in transient absorption rate. DTA does not require for saturated absorption (Figure 8e2,3). Gaussian and doughnut-shaped pumps with relatively low intensity are applied respectively and a probe beam is utilized to obtain transient absorption signals. Subtraction of the signal by doughnut pump from that by Gaussian pump will result in a significantly shrunken spatial PSF (refer to Table 1 for the equation).

Saturated excitation microscopy (SAX) is another type of pump–probe microscopy. In the saturated illumination condition, it has been found that the excited fluorescence is proportional to the temporal dynamic which is the superposition of an exponential decay and a constant value.[228,229] At any position throughout the fluorescence center to the periphery, the decay rate is proportional to the excitation intensity. This theoretical law has been verified by experiments, which is beneficial for spatial resolution improvement. However, saturation absorption normally induces high risk of photodamage to the living samples. In order to further reduce the reciprocal side-effect, which routinely contaminates the resulting imaging quality, differential SAX (dSAX) has been proposed.[62,230] As we know, the fluorescence intensity varies under different saturation excitation intensities. And because nonlinear component is determined by the differentiation between the estimated linear fluorescence intensity and the factual fluorescence intensity, the subtraction of the latter from the former will result in the PSF of nonlinear component, which presents sharper profile in contrast to linear component. The experimental research has demonstrated its superiority in image quality with less photobleaching effect. Nonetheless, this differential excitation technique is hindered by sample drifting and laser power fluctuation. Subtraction technique is also useful for dual-color imaging in SAX.[183] In cell samples stained with easily-bleached organic dyes and nonbleaching FNDs, after bleaching of the organic dyes, targets labeled with FNDs alone are obtained. By subtracting image after bleaching from that before bleaching, the image stained with organic fluorophores can be achieved.

5. Conclusion

It is noteworthy that the existing subdiffracted microscopic techniques are not feasible in many applications due to shortcomings, like difficult implementation and high cost. Solutions, such as digital image process, fluorescent dye modification, optical setup optimization and so on, are developed to address the issues. Our reviewing work is focusing on the optimization of current super-resolved versions so that they could be broadly applied to biological community. Improvement in factors, like hardware, light path, probes, and algorithm, are involved. In the midst of those strategies, subtraction technique is relatively cheap and easily-implemented. Subtractive super-resolution imaging (SSRI) has been widely used in biological and material science, as well as in the nonlinear optical imaging. A comparison of the applications of each SSRI technique is presented based on the spatial and temporal specifics (**Figure 9**). Life science researchers should select the most suitable technique according to the requirement of the living specimens. **Figure 10** gives a summary of the subtractive rationales based on PSF engineering. Note that the resolution improvement of each SSRI method could be expounded via the intensity relationship analysis of the differential components. In a point-scanning scheme, different pinhole sizes could produce different resulting PSFs. As such, performing a subtraction between these solid PSFs will yield resolution-enhanced images (Figure 10a–c).[28] In the widefield scheme, phase masks are substitutable to pinholes. Subtraction of images obtained by different phase masks with different patterns will similarly ameliorate the final image quality (Figure 10e).[80] Apart from the far-field condition, subtraction technique is expedient for some near-field imaging, like supercritical angle fluorescence microscopy (SAF) or superoscillation microscopy (Figure 10d).[81,231] Recently, extended applications of subtraction technique in other imaging techniques, including nonlinear optical microscopy, have shown an upward trend. It is expected that commercial optical super-resolution microscopy setup will be available for cell research and material science community in the future, achieving ultrahigh 3D resolution and real time imaging without compromise.

Note that subtraction technique possesses the drawback of doubling of the acquisition time. Detector array adds versatility to the subtraction technique. In a parallel detection scheme, a single detector is replaced by the detector array and the resulting image can be obtained with only one scan. After pixel reassignment, inner ring point-detectors form a solid-profiled PSF image while outer ring point-detectors generate a hollow-profiled PSF image (Figure 10f–j). Subtraction of the two yields the final resolution at a factor of 2. In our perspective, based on subtraction technique, detector array microscopy will be a fashion in subcellular research field because of its versatile setup, high acquisition speed, and relatively high spatial 3D resolution.[4] For example, MINFLUX is a promising approach for achieving nanoscale localization with minimal photon flux; however, for each molecular localization, it requires four illuminations, which greatly decreases the acquisition speed.[140] Using a detector array scheme,

© 2020 Wiley-VCH GmbH

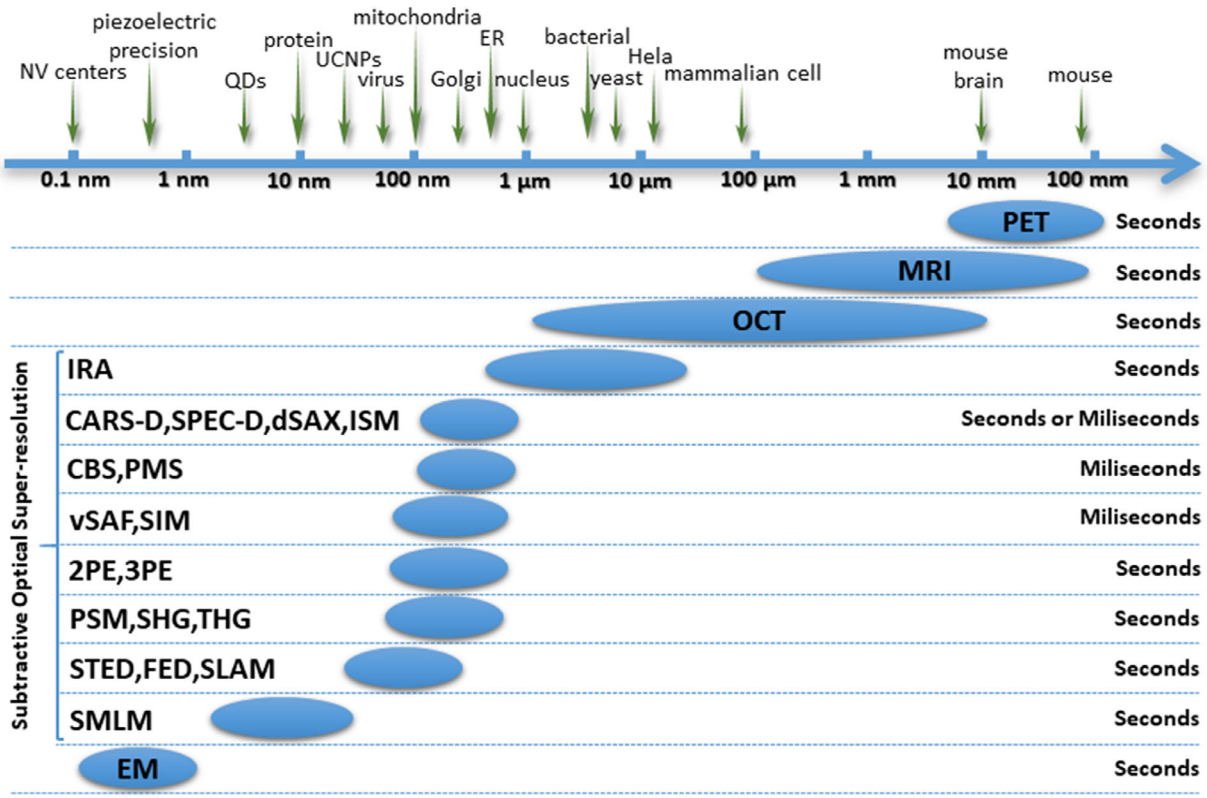

Figure 9. Spatial and temporal resolution comparison concerning the subtractive optical super-resolution microscopy. Reproduced with permission.[233] Copyright 2008, Springer Nature. PET: positron-emission tomography; MRI: magnetic resonance imaging; OCT: optical coherence tomography; EM: electron microscopy; ER: endoplasmic reticulum.

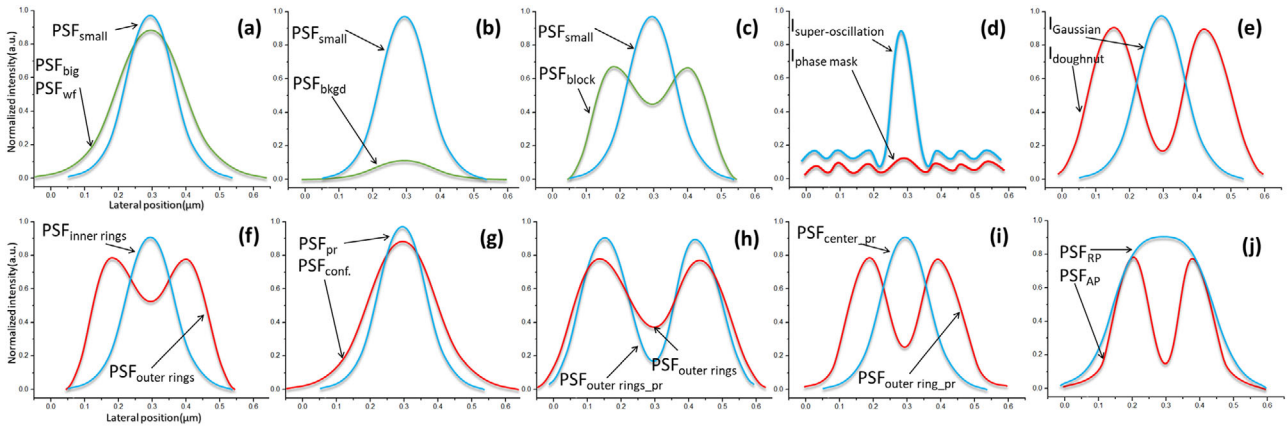

Figure 10. Schematic overview of PSF engineering in the improvement of super-resolution microscopy. a–c) Pinhole-dependent differential microscopy. d) The subtraction methods applied in near-field microscopy. e) Subtraction methods in widefield microscopy, like phase mask subtraction (PMS) or wavefront subtraction (WSM). f–i) The subtraction strategies applied in photon reassignment, like image scanning microscopy (ISM) or detector array microscopy (DA). j) Switching laser mode differential method. Refer to **Table 1** for detailed information.

with only one illumination, the subtraction of fluorescence signals from an inner-ring detector and an outer-ring detector could achieve molecular localization.

Supporting Information

Supporting Information is available from the Wiley Online Library or from the author.

Acknowledgements

C.L. and V.L. contributed equally to this work. This research was funded by the National Natural Science Foundation of China (61827825 and 61735017), Key Research and Development Program of Zhejiang Province (2020C01116), Fundamental Research Funds for the Central Universities (2019XZZX003-06 and K20200132), and Zhejiang Lab (2018EB0ZX01 and 2020MC0AE01).

© 2020 Wiley-VCH GmbH

Conflict of Interest

The authors declare no conflict of interest.

Keywords

background suppression, nonlinear optical imaging, photon reassignment, subtraction technique, super-resolution microscopy

Received: March 8, 2019
Revised: September 29, 2020
Published online:

[1] E. Abbe, *Arch. Mikrosk. Anat.* **1873**, *9*, 413.
[2] M. A. A. Neil, R. Juskaitis, T. Wilson, *Opt. Lett.* **1997**, *22*, 1905.
[3] T. Wilson, *J. Microsc.* **2011**, *244*, 113.
[4] C. K. Li, C. F. Kuang, X. Liu, *ACS Nano* **2018**, *12*, 4081.
[5] C. Kuang, S. Li, W. Liu, X. Hao, Z. Gu, Y. Wang, J. Ge, H. Li, X. Liu, *Sci. Rep.* **2013**, *3*, 1441.
[6] M. Castello, G. Tortarolo, M. Buttafava, T. Deguchi, F. Villa, S. Koho, L. Pesce, M. Oneto, S. Pelicci, L. Lanzano, P. Bianchini, C. J. R. Sheppard, A. Diaspro, A. Tosi, G. Vicidomini, *Nat. Methods* **2019**, *16*, 175.
[7] S. W. Hell, J. Wichmann, *Opt. Lett.* **1994**, *19*, 780.
[8] G. Vicidomini, G. Moneron, K. Y. Han, V. Westphal, H. Ta, M. Reuss, J. Engelhardt, C. Eggeling, S. W. Hell, *Nat. Methods* **2011**, *8*, 571.
[9] C. Li, S. Liu, W. Wang, W. Liu, C. Kuang, X. Liu, *J. Microsc.* **2018**, *271*, 4.
[10] S. J. Sahl, S. W. Hell, S. Jakobs, *Nat. Rev. Mol. Cell Biol.* **2017**, *18*, 685.
[11] T. Staudt, A. Engler, E. Rittweger, B. Harke, J. Engelhardt, S. W. Hell, *Opt. Express* **2011**, *19*, 5644.
[12] F. Gottfert, T. Pleiner, J. Heine, V. Westphal, D. Gorlich, S. J. Sahl, S. W. Hell, *Proc. Natl. Acad. Sci. USA* **2017**, *114*, 2125.
[13] J. Heine, M. Reuss, B. Harke, E. D'Este, S. J. Sahl, S. W. Hell, *Proc. Natl. Acad. Sci. USA* **2017**, *114*, 9797.
[14] G. Vicidomini, G. Moneron, C. Eggeling, E. Rittweger, S. W. Hell, *Opt. Express* **2012**, *20*, 5225.
[15] E. Ronzitti, B. Harke, A. Diaspro, *Opt. Express* **2013**, *21*, 210.
[16] J. Hanne, H. J. Falk, F. Gorlitz, P. Hoyer, J. Engelhardt, S. J. Sahl, S. W. Hell, *Nat. Commun.* **2015**, *6*, 7127.
[17] L. Lanzano, I. Coto Hernandez, M. Castello, E. Gratton, A. Diaspro, G. Vicidomini, *Nat. Commun.* **2015**, *6*, 6701.
[18] M. Castello, G. Tortarolo, I. Coto Hernandez, T. Deguchi, A. Diaspro, G. Vicidomini, *Rev. Sci. Instrum.* **2017**, *88*, 053701.
[19] P. Gao, G. U. Nienhaus, *Opt. Lett.* **2017**, *42*, 831.
[20] C. K. Li, Y. H. Li, Y. B. Han, Z. M. Zhang, Y. Z. Li, W. S. Wang, X. Hao, C. F. Kuang, X. Liu, *ACS Photonics* **2020**, *7*, 1788.
[21] X. D. Chen, C. L. Zou, Z. J. Gong, C. H. Dong, G. C. Guo, F. W. Sun, *Light: Sci. Appl.* **2015**, *4*, 1.
[22] R. J. Stoehr, R. Kolesov, K. Xia, R. Reuter, J. Meijer, G. Logvenov, J. Wrachtrup, *ACS Nano* **2012**, *6*, 9175.
[23] B. Yang, J. B. Trebbia, R. Baby, P. Tamarat, B. Lounis, *Nat. Photonics* **2015**, *9*, 658.
[24] M. J. Rust, M. Bates, X. Zhuang, *Nat. Methods* **2006**, *3*, 793.
[25] E. Betzig, G. H. Patterson, R. Sougrat, O. W. Lindwasser, S. Olenych, J. S. Bonifacino, M. W. Davidson, J. Lippincott-Schwartz, H. F. Hess, *Science* **2006**, *313*, 1642.
[26] M. G. L. Gustafsson, *J. Microsc.* **2000**, *198*, 82.
[27] L. Zhu, W. Zhang, D. Elnatan, B. Huang, *Nat. Methods* **2012**, *9*, 721.
[28] R. Heintzmann, V. Sarafis, P. Munroe, J. Nailon, Q. S. Hanley, T. M. Jovin, *Micron* **2003**, *34*, 293.
[29] H. Okugawa, *Proc. SPIE* **2008**, *6860*, 68600K.
[30] A. R. Halpern, G. C. M. Alas, T. J. Chozinski, A. R. Paredez, J. C. Vaughan, *ACS Nano* **2017**, *11*, 12677.
[31] X. Sun, Z. Liu, K. Welsher, J. T. Robinson, A. Goodwin, S. Zaric, H. Dai, *Nano Res.* **2008**, *1*, 203.
[32] R. Zanella, G. Zanghirati, R. Cavicchioli, L. Zanni, P. Boccacci, M. Bertero, G. Vicidomini, *Sci. Rep.* **2013**, *3*, 2523.
[33] C. H. Lee, J. P. Wang, *Opt. Commun.* **1997**, *135*, 233.
[34] X. Hao, C. Kuang, Z. Gu, S. Li, J. Ge, X. Liu, *Opt. Lett.* **2013**, *38*, 1001.
[35] Y. Fang, Y. F. Wang, C. F. Kuang, X. Liu, *Opt. Commun.* **2014**, *322*, 169.
[36] C. Chen, F. Wang, S. Wen, Q. P. Su, M. C. L. Wu, Y. Liu, B. Wang, D. Li, X. Shan, M. Kianinia, I. Aharonovich, M. Toth, S. P. Jackson, P. Xi, D. Jin, *Nat. Commun.* **2018**, *9*, 3290.
[37] Q. Wu, B. Huang, X. Peng, S. He, Q. Zhan, *Opt. Express* **2017**, *25*, 30885.
[38] W. S. Wang, G. Y. Zhao, C. F. Kuang, L. Xu, S. C. Liu, S. Y. Sun, S. T. Ping, Y. Yang, Y. K. Xu, X. Liu, *Opt. Commun.* **2018**, *423*, 167.
[39] S. Xiao, J. Mertz, *Biomed. Opt. Express* **2019**, *10*, 2467.
[40] Y. F. Wang, C. F. Kuang, H. Q. Cai, S. Li, W. Liu, X. Hao, J. H. Ge, X. Liu, *Opt. Commun.* **2014**, *312*, 62.
[41] R. Chapman, T. Plakhotnik, *Opt. Lett.* **2013**, *38*, 1847.
[42] J. Storteboom, P. Dolan, S. Castelletto, X. Li, M. Gu, *Opt. Express* **2015**, *23*, 11327.
[43] R. Igarashi, Y. Yoshinari, H. Yokota, T. Sugi, F. Sugihara, K. Ikeda, H. Sumiya, S. Tsuji, I. Mori, H. Tochio, Y. Harada, M. Shirakawa, *Nano Lett.* **2012**, *12*, 5726.
[44] A. Hegyi, E. Yablonovitch, *Nano Lett.* **2013**, *13*, 1173.
[45] K. Korobchevskaya, C. Peres, Z. Li, A. Antipov, C. J. Sheppard, A. Diaspro, P. Bianchini, *Sci. Rep.* **2016**, *6*, 25816.
[46] W. Zhao, J. Tan, L. Qiu, *Opt. Express* **2004**, *12*, 5191.
[47] W. Q. Zhao, J. B. Tan, L. R. Qiu, L. M. Zou, *Meas. Sci. Technol.* **2005**, *16*, 497.
[48] J. Liu, J. Tan, H. Bin, Y. Wang, *Appl. Opt.* **2009**, *48*, 6195.
[49] A. Ourjoumtsev, A. Dantan, R. Tualle-Brouri, P. Grangier, *Phys. Rev. Lett.* **2007**, *98*, 030502.
[50] G. Brida, L. Caspani, A. Gatti, M. Genovese, A. Meda, I. R. Berchera, *Phys. Rev. Lett.* **2009**, *102*, 213602.
[51] L. Wang, J. Xia, J. Yao, K. I. Maslov, L. V. Wang, *Phys. Rev. Lett.* **2013**, *111*, 204301.
[52] L. Wang, C. Zhang, L. V. Wang, *Phys. Rev. Lett.* **2014**, *113*, 174301.
[53] P. Hosseini, R. Zhou, Y.-H. Kim, C. Peres, A. Diaspro, C. Kuang, Z. Yaqoob, P. T. C. So, *Opt. Lett.* **2016**, *41*, 1656.
[54] S. P. Poland, A. T. Erdogan, N. Krstajic, J. Levitt, V. Devauges, R. J. Walker, D. D. Li, S. M. Ameer-Beg, R. K. Henderson, *Opt. Express* **2016**, *24*, 6899.
[55] B. P. Jena, D. L. Gatti, S. Arslanturk, S. Pernal, D. J. Taatjes, *Micron* **2019**, *117*, 55.
[56] J. Lee, I. Kolb, C. R. Forest, C. J. Rozell, *IEEE Trans. Image Process.* **2018**, *27*, 1847.
[57] G. Young, N. Hundt, D. Cole, A. Fineberg, J. Andrecka, A. Tyler, A. Olerinyova, A. Ansari, E. G. Marklund, M. P. Collier, S. A. Chandler, O. Tkachenko, J. Allen, M. Crispin, N. Billington, Y. Takagi, J. R. Sellers, C. Eichmann, P. Selenko, L. Frey, R. Riek, M. R. Galpin, W. B. Struwe, J. L. P. Benesch, P. Kukura, *Science* **2018**, *360*, 423.
[58] S. Yue, M. N. Slipchenko, J. X. Cheng, *Laser Photonics Rev.* **2011**, *5*, 496.
[59] A. Leray, K. Lillis, J. Mertz, *Biophys. J.* **2008**, *94*, 1449.
[60] D. Wang, S. Liu, Y. Chen, J. Song, W. Liu, M. Xiong, G. Wang, X. Peng, J. Qu, *Opt. Express* **2017**, *25*, 10276.
[61] I. Pita, N. Hendaoui, N. Liu, M. Kumbham, S. A. M. Tofail, A. Peremans, C. Silien, *Opt. Express* **2013**, *21*, 25632.
[62] Y. Nawa, Y. Yonemaru, A. Kasai, R. Oketani, H. Hashimoto, N. I. Smith, K. Fujita, *APL Photonics* **2018**, *3*, 080805.
[63] N. Tian, L. Fu, M. Gu, *Sci. Rep.* **2015**, *5*, 13580.

© 2020 Wiley-VCH GmbH

[64] W. Min, C. W. Freudiger, S. Lu, X. S. Xie, *Annu. Rev. Phys. Chem.* **2011**, *62*, 507.
[65] M. Gao, R. Maraspini, O. Beutel, A. Zehtabian, B. Eickholt, A. Honigmann, H. Ewers, *ACS Nano* **2018**, *12*, 4178.
[66] R. Li, X. Chen, Z. Lin, Y. Wang, Y. Sun, *Nanoscale* **2018**, *10*, 7552.
[67] N. Wang, T. Kobayashi, *Opt. Express* **2014**, *22*, 28819.
[68] S. J. Hewlett, T. Wilson, *Mach. Vis. Appl.* **1991**, *4*, 233.
[69] E. Sanchez-Ortiga, C. J. R. Sheppard, G. Saavedra, M. Martinez-Corral, A. Doblas, A. Calatayud, *Opt. Lett.* **2012**, *37*, 1280.
[70] Y. H. Chen, D. Z. Zhu, Y. Fang, C. F. Kuang, X. Liu, *Opt. Commun.* **2017**, *404*, 184.
[71] B. Ge, Y. Ma, C. Kuang, D. Zhang, K. C. Toussaint, Jr., S. You, X. Liu, *Opt. Express* **2015**, *23*, 13159.
[72] D. Zhu, W. Liu, Z. Zhang, C. Zheng, Y. Chen, C. Li, C. Kuang, J. Fan, Y. Xu, X. Liu, A. Hussain, *J. Microsc.* **2018**, *272*, 151.
[73] S. Sun, S. Liu, C. Kuang, X. Liu, *Appl. Opt.* **2017**, *56*, 3799.
[74] M. Kumbham, R. Mouras, A. Mani, S. Daly, K. O'Dwyer, A. Toma, P. Bianchini, A. N. Diaspro, S. A. M. Liu Tofail, C. Silien, *Opt. Express* **2017**, *25*, 13145.
[75] T. Wilson, D. K. Hamilton, *Opt. Acta* **1984**, *31*, 453.
[76] R. Gauderon, C. J. R. Sheppard, *Bioimaging* **1998**, *6*, 126.
[77] Y. Ma, C. Kuang, W. Gong, L. Xue, Y. Zheng, Y. Wang, K. Si, X. Liu, *Appl. Opt.* **2015**, *54*, 1354.
[78] V. N. Le, S. Q. Chen, Z. G. Fan, N. M. Pham, *Appl. Opt.* **2016**, *55*, 1067.
[79] L. V. Nhu, Z. Fan, S. Chen, F. Dang, *Appl. Opt.* **2016**, *55*, 7345.
[80] Y. Han, C. Zhang, *Opt. Lett.* **2010**, *35*, 2115.
[81] T. Barroca, K. Balaa, S. Leveque-Fort, E. Fort, *Phys. Rev. Lett.* **2012**, *108*, 218101.
[82] K. Huang, F. Qin, H. Liu, H. Ye, C.-W. Qiu, M. Hong, B. Luk'yanchuk, J. Teng, *Adv. Mater.* **2018**, *30*, 1704556.
[83] H. Q. Cai, Y. F. Wang, C. F. Kuang, J. H. Ge, Y. K. Xu, X. Liu, *J. Mod. Opt.* **2015**, *62*, 1223.
[84] C. B. Muller, J. Enderlein, *Phys. Rev. Lett.* **2010**, *104*, 198101.
[85] G. M. R. De Luca, R. M. P. Breedijk, R. A. J. Brandt, C. H. C. Zeelenberg, B. E. de Jong, W. Timmermans, L. N. Azar, R. A. Hoebe, S. Stallinga, E. M. M. Manders, *Biomed. Opt. Express* **2013**, *4*, 2644.
[86] S. Roth, C. J. Sheppard, W. Kai, R. Heintzmann, *Opt. Nanosc.* **2013**, *2*, 5.
[87] C. J. R. Sheppard, S. B. Mehta, R. Heintzmann, *Opt. Lett.* **2013**, *38*, 2889.
[88] T. Azuma, T. Kei, *Opt. Express* **2015**, *23*, 15003.
[89] J. Huff, *Nat. Methods* **2016**, *13*, 958.
[90] C. Kuang, Y. Ma, R. Zhou, G. Zheng, Y. Fang, Y. Xu, X. Liu, P. T. C. So, *Phys. Rev. Lett.* **2016**, *117*, 028102.
[91] Y. Li, S. Liu, D. Liu, S. Sun, C. Kuang, Z. Ding, X. Liu, *J. Microsc.* **2017**, *266*, 288.
[92] S. Liu, S. Sun, C. Kuang, B. Ge, W. Wang, X. Liu, *Opt. Commun.* **2017**, *395*, 45.
[93] B. Ge, Y. Wang, Y. Huang, C. Kuang, Y. Fang, P. Xiu, Z. Rong, X. Liu, *Opt. Lett.* **2016**, *41*, 2013.
[94] R. Tenne, U. Rossman, B. Rephael, Y. Israel, A. Krupinski-Ptaszek, R. Lapkiewicz, Y. Silberberg, D. Oron, *Nat. Photonics* **2019**, *13*, 116.
[95] O. Haeberle, B. Simon, *Opt. Commun.* **2009**, *282*, 3657.
[96] H. Dehez, M. Piche, Y. De Koninck, *Opt. Express* **2013**, *21*, 15912.
[97] Y. Gan, M. He, Z. Zhang, S. Liu, L. Xu, X. Hao, C. Kuang, X. Liu, *Appl. Opt.* **2019**, *58*, 9069.
[98] Y. Wang, Y. Ma, C. Kuang, Y. Fang, Y. Xu, X. Liu, Z. Ding, *Appl. Opt.* **2015**, *54*, 5425.
[99] H. Jia, X. Yu, Y. Yang, X. Zhou, S. Yan, C. Liu, M. Lei, B. Yao, *J. Biophotonics* **2018**, *12*, 201800094.
[100] S. Li, C. F. Kuang, X. Hao, Y. F. Wang, J. H. Ge, X. Liu, *J. Opt.* **2013**, *15*, 5708.
[101] S. Segawa, Y. Kozawa, S. Sato, *Opt. Lett.* **2014**, *39*, 3118.
[102] S. You, C. Kuang, Z. Rong, X. Liu, *Opt. Express* **2014**, *22*, 26375.
[103] N. Wang, T. Kobayashi, *Opt. Express* **2015**, *23*, 13704.
[104] N. Wang, T. Kobayashi, *Opt. Express* **2015**, *23*, 13410.
[105] J. Kim, D. Kim, S. Back, *Microsc. Res. Tech.* **2009**, *72*, 441.
[106] Y. Kozawa, T. Hibi, A. Sato, H. Horanai, M. Kurihara, N. Hashimoto, H. Yokoyama, T. Nemoto, S. Sato, *Opt. Express* **2011**, *19*, 15947.
[107] K. Youngworth, T. Brown, *Opt. Express* **2000**, *7*, 77.
[108] G. Zhao, C. Kuang, Z. Ding, X. Liu, *Opt. Express* **2016**, *24*, 23596.
[109] J.-r. Choi, S. Lee, K. Kim, *Biomed. Eng. Lett.* **2014**, *4*, 231.
[110] D. Solis, Jr., W.-S. Chang, B. P. Khanal, K. Bao, P. Nordlander, E. R. Zubarev, S. Link, *Nano Lett.* **2010**, *10*, 3482.
[111] B. Ge, L. Zhu, C. Kuang, D. Zhang, Y. Fang, Y. Ma, X. Liu, *Opt. Express* **2015**, *23*, 32561.
[112] K. Jiang, X. Lei, K. Li, Y. Lu, P. Wang, *Opt. Express* **2018**, *26*, 2380.
[113] S. Cao, W. Cai, Q. Liu, Y. Li, *Annu. Rev. Anal. Chem.* **2012**, *5*, 317.
[114] E. Cortes, P. A. Huidobro, H. G. Sinclair, S. Guldbrand, W. J. Peveler, T. Davies, S. Parrinello, F. Gorlitz, C. Dunsby, M. A. A. Neil, Y. Sivan, I. P. Parkin, P. M. W. French, S. A. Maier, *ACS Nano* **2016**, *10*, 10454.
[115] J. L. Ponsetto, F. Wei, Z. Liu, *Nanoscale* **2014**, *6*, 5807.
[116] K. L. Blythe, E. J. Titus, K. A. Willets, *J. Phys. Chem. C* **2015**, *119*, 19333.
[117] K. A. Willets, A. J. Wilson, V. Sundaresan, P. B. Joshi, *Chem. Rev.* **2017**, *117*, 7538.
[118] T. Ichimura, N. Hayazawa, M. Hashimoto, Y. Inouye, S. Kawata, *Phys. Rev. Lett.* **2004**, *92*, 220801.
[119] N. Accanto, L. Piatkowski, I. M. Hancu, J. Renger, N. F. van Hulst, *Appl. Phys. Lett.* **2016**, *108*, 083115.
[120] H. Zhang, M. Zhao, L. Peng, *Opt. Express* **2011**, *19*, 24783.
[121] Q. Li, H. Wei, H. Xu, *Nano Lett.* **2015**, *15*, 8181.
[122] P. Yuan, Y. H. Lee, M. K. Gnanasammandhan, Z. Guan, Y. Zhang, Q.-H. Xu, *Nanoscale* **2012**, *4*, 5132.
[123] Y. Y. Hui, Y.-C. Lu, L.-J. Su, C.-Y. Fang, J.-H. Hsu, H.-C. Chang, *Appl. Phys. Lett.* **2013**, *102*, 093501.
[124] K. Kim, Y. Oh, W. Lee, D. Kim, *Opt. Lett.* **2010**, *35*, 3501.
[125] H. Shen, E. Huang, T. Das, H. Xu, M. Ellisman, Z. Liu, *Opt. Express* **2014**, *22*, 10728.
[126] L. Xiao, L. Wei, X. Cheng, Y. He, E. S. Yeung, *Anal. Chem.* **2011**, *83*, 7340.
[127] W. T. Tang, E. Chung, Y.-H. Kim, P. T. C. So, C. J. R. Sheppard, *Opt. Lett.* **2010**, *35*, 517.
[128] F. R. Winter, M. Loidolt, V. Westphal, A. N. Butkevich, C. Gregor, S. J. Sahl, S. W. Hell, *Sci. Rep.* **2017**, *7*, 46492.
[129] S. Galiani, B. Harke, G. Vicidomini, G. Lignani, F. Benfenati, A. Diaspro, P. Bianchini, *Opt. Express* **2012**, *20*, 7362.
[130] I. Coto Hernandez, C. Peres, F. Cella Zanacchi, M. d'Amora, S. Christodoulou, P. Bianchini, A. Diaspro, G. Vicidomini, *J. Biophotonics* **2014**, *7*, 376.
[131] N. Chen, C.-H. Wong, C. J. R. Sheppard, *Opt. Express* **2008**, *16*, 18764.
[132] P. Gao, B. Prunsche, L. Zhou, K. Nienhaus, G. U. Nienhaus, *Nat. Photonics* **2017**, *11*, 163.
[133] J.-C. Lee, Y. Ma, K. Y. Han, T. Ha, *ACS Photonics* **2019**, *6*, 1189.
[134] J. Schneider, J. Zahn, M. Maglione, S. J. Sigrist, J. Marquard, J. Chojnacki, H. G. Krausslich, S. J. Sahl, J. Engelhardt, S. W. Hell, *Nat. Methods* **2015**, 12.
[135] A. Pereira, M. Sousa, A. C. Almeida, L. T. Ferreira, A. R. Costa, M. Novais-Cruz, C. Ferras, M. M. Sousa, P. Sampaio, M. Belsley, H. Maiato, *Opt. Express* **2019**, *27*, 8092.
[136] M. Castello, A. Diaspro, G. Vicidomini, *Appl. Phys. Lett.* **2014**, *105*, 234106.
[137] Y. Wu, X. Wu, L. Toro, E. Stefani, *Methods* **2015**, *88*, 48.
[138] C. Spahn, J. B. Grimm, L. D. Lavis, M. Lampe, M. Heilemann, *Nano Lett.* **2019**, *19*, 500.
[139] M. Lakadamyali, *ChemPhysChem* **2014**, *15*, 630.

© 2020 Wiley-VCH GmbH

[140] F. Balzarotti, Y. Eilers, K. C. Gwosch, A. H. Gynna, V. Westphal, F. D. Stefani, J. Elf, S. W. Hell, *Science* **2017**, *355*, 606.
[141] Y. Eilers, H. Ta, K. C. Gwosch, F. Balzarotti, S. W. Hell, *Proc. Natl. Acad. Sci. USA* **2018**, *115*, 6117.
[142] M. P. Gordon, T. Ha, P. R. Selvin, *Proc. Natl. Acad. Sci. USA* **2004**, *101*, 6462.
[143] P. D. Simonson, E. Rothenberg, P. R. Selvin, *Nano Lett.* **2011**, *11*, 5090.
[144] X. Qu, D. Wu, L. Mets, N. F. Scherer, *Proc. Natl. Acad. Sci. USA* **2004**, *101*, 11298.
[145] P. Delcanale, B. Miret-Ontiveros, M. Arista-Romero, S. Pujals, L. Albertazzi, *ACS Nano* **2018**, *12*, 7629.
[146] D. T. Burnette, P. Sengupta, Y. Dai, J. Lippincott-Schwartz, B. Kachar, *Proc. Natl. Acad. Sci. USA* **2011**, *108*, 21081.
[147] S. Munck, K. Miskiewicz, R. Sannerud, S. A. Menchon, L. Jose, R. Heintzmann, P. Verstreken, W. Annaert, *J. Cell Sci.* **2012**, *125*, 2257.
[148] Y. Chen, W. Liu, Z. Zhang, C. Zheng, Y. Huang, R. Cao, D. Zhu, L. Xu, M. Zhang, Y. H. Zhang, J. Fan, L. Jin, Y. Xu, C. Kuang, X. Liu, *Nat. Commun.* **2018**, *9*, 4818.
[149] O. Mandula, M. Kielhorn, K. Wicker, G. Krampert, I. Kleppe, R. Heintzmann, *Opt. Express* **2012**, *20*, 24167.
[150] R. Heintzmann, T. M. Jovin, C. Cremer, *J. Opt. Soc. Am. A* **2002**, *19*, 1599.
[151] R. Heintzmann, *Micron* **2003**, *34*, 283.
[152] A. G. York, S. H. Parekh, D. D. Nogare, R. S. Fischer, K. Temprine, M. Mione, A. B. Chitnis, C. A. Combs, H. Shroff, *Nat. Methods* **2012**, *9*, 749.
[153] E. N. Ward, F. H. Torkelsen, R. Pal, *R. Soc. Open Sci.* **2018**, *5*, 171336.
[154] M. Ingaramo, A. G. York, P. Wawrzusin, O. Milberg, A. Hong, R. Weigert, H. Shroff, G. H. Patterson, *Proc. Natl. Acad. Sci. USA* **2014**, *111*, 5254.
[155] P. Vermeulen, H. Zhan, F. Orieux, J. C. Olivo-Marin, Z. Lenkei, V. Loriette, A. Fragola, *J. Microsc.* **2015**, *259*, 257.
[156] Z. H. Rong, S. Li, C. F. Kuang, Y. K. Xu, X. Liu, *J. Mod. Opt.* **2014**, *61*, 1364.
[157] R. Gao, S. M. Asano, S. Upadhyayula, I. Pisarev, D. E. Milkie, T.-L. Liu, V. Singh, A. Graves, G. H. Huynh, Y. Zhao, J. Bogovic, J. Colonell, C. M. Ott, C. Zugates, S. Tappan, A. Rodriguez, K. R. Mosaliganti, S.-H. Sheu, H. A. Pasolli, S. Pang, C. S. Xu, S. G. Megason, H. Hess, J. Lippincott-Schwartz, A. Hantman, G. M. Rubin, T. Kirchhausen, S. Saalfeld, Y. Aso, E. S. Boyden, E. Betzig, *Science* **2019**, *363*, 1.
[158] D. Oron, Y. Silberberg, *Opt. Express* **2005**, *13*, 9903.
[159] P. W. Winter, H. Shroff, *Curr. Opin. Chem. Biol.* **2014**, *20*, 46.
[160] M. D. Bordenave, F. Balzarotti, F. D. Stefani, S. W. Hell, *J. Phys. D: Appl. Phys.* **2016**, *49*, 365102.
[161] Y. Ma, C. Kuang, Y. Fang, B. Ge, D. Li, X. Liu, *Opt. Lett.* **2015**, *40*, 4627.
[162] D. Zhu, Y. Chen, C. Kuang, X. Liu, *Opt. Commun.* **2017**, *395*, 29.
[163] B. Huang, Q. Wu, X. Peng, L. Yao, D. Peng, Q. Zhan, *Nanoscale* **2018**, *10*, 21025.
[164] S. Sun, M. He, Z. Zhang, W. Wang, X. Yang, C. Kuang, X. Liu, *Appl. Opt.* **2019**, *58*, 4892.
[165] P. J. Keller, M. B. Ahrens, *Neuron* **2015**, *85*, 462.
[166] W. J. Liu, K. C. Toussaint, C. Okoro, D. Z. Zhu, Y. H. Chen, C. F. Kuang, X. Liu, *Laser Photonics Rev.* **2018**, *12*, 1700333.
[167] R. Schmidt, C. A. Wurm, S. Jakobs, J. Engelhardt, A. Egner, S. W. Hell, *Nat. Methods* **2008**, *5*, 539.
[168] I. Testa, N. T. Urban, S. Jakobs, C. Eggeling, K. I. Willig, S. W. Hell, *Neuron* **2012**, *75*, 992.
[169] B. Huang, W. Wang, M. Bates, X. Zhuang, *Science* **2008**, *319*, 810.
[170] L. Shao, P. Kner, E. H. Rego, M. G. L. Gustafsson, *Nat. Methods* **2011**, *8*, 1044.
[171] M. G. Gustafsson, L. Shao, P. M. Carlton, C. J. Wang, I. N. Golubovskaya, W. Z. Cande, D. A. Agard, J. W. Sedat, *Biophys. J.* **2008**, *94*, 4957.
[172] M. F. Juette, T. J. Gould, M. D. Lessard, M. J. Mlodzianoski, B. S. Nagpure, B. T. Bennett, S. T. Hess, J. Bewersdorf, *Nat. Methods* **2008**, *5*, 527.
[173] S. R. P. Pavani, M. A. Thompson, J. S. Biteen, S. J. Lord, N. Liu, R. J. Twieg, R. Piestun, W. E. Moerner, *Proc. Natl. Acad. Sci. USA* **2009**, *106*, 2995.
[174] S. Jia, J. C. Vaughan, X. Zhuang, *Nat. Photonics* **2014**, *8*, 302.
[175] Y. Wang, G. Fruhwirth, E. Cai, T. Ng, P. R. Selvin, *Nano Lett.* **2013**, *13*, 5233.
[176] J. Xu, K. F. Tehrani, P. Kner, *ACS Nano* **2015**, *9*, 2917.
[177] D. Z. Zhu, Y. H. Chen, Y. Fang, A. Hussain, C. F. Kuang, X. X. Zhou, Y. K. Xu, X. Liu, *Opt. Commun.* **2017**, *405*, 157.
[178] N. Wang, T. Kobayashi, *J. Opt.* **2015**, *17*, 125302.
[179] S. T. You, C. F. Kuang, S. Li, X. Liu, Z. H. Ding, *AIP Adv.* **2015**, *5*, 084901.
[180] V. Le, X. N. Wang, C. F. Kuang, X. Liu, *Opt. Eng.* **2018**, *57*, 103107.
[181] X. Z. Lim, *Nature* **2016**, *531*, 26.
[182] D. Jin, P. Xi, B. Wang, L. Zhang, J. Enderlein, A. M. van Oijen, *Nat. Methods* **2018**, *15*, 415.
[183] Y. Masahito, T. Yan-Kai, K. Shogo, N. I. Smith, K. Satoshi, H. C. Chang, F. Katsumasa, *Biomed. Opt. Express* **2011**, *2*, 1946.
[184] X. Michalet, F. F. Pinaud, L. A. Bentolila, J. M. Tsay, S. Doose, J. J. Li, G. Sundaresan, A. M. Wu, S. S. Gambhir, S. Weiss, *Science* **2005**, *307*, 538.
[185] I. L. Medintz, H. T. Uyeda, E. R. Goldman, H. Mattoussi, *Nat. Methods* **2005**, *4*, 435.
[186] S. E. Irvine, T. Staudt, E. Rittweger, J. Engelhardt, S. W. Hell, *Angew. Chem.* **2008**, *47*, 2685.
[187] M. D. Lesoine, U. Bhattacharjee, Y. J. Guo, J. Vela, J. W. Petrich, E. A. Smith, *J. Phys. Chem. C* **2013**, *117*, 3662.
[188] S. Ye, W. Yan, M. Zhao, X. Peng, J. Song, J. Qu, *Adv. Mater.* **2018**, *30*, 1800167.
[189] T. Kaldewey, A. V. Kuhlmann, S. R. Valentin, A. Ludwig, A. D. Wieck, R. J. Warburton, *Nat. Photonics* **2018**, *12*, 68.
[190] Q. Zhan, H. Liu, B. Wang, Q. Wu, R. Pu, C. Zhou, B. Huang, X. Peng, H. Agren, S. He, *Nat. Commun.* **2017**, *8*, 1058.
[191] W. Fan, W. Bu, J. Shi, *Adv. Mater.* **2016**, *28*, 3987.
[192] Y. Y. Hui, W. W. W. Hsiao, S. Haziza, M. Simonneau, F. Treussart, H. C. Chang, *Curr. Opin. Solid State Mater. Sci.* **2017**, *21*, 35.
[193] L. P. McGuinness, Y. Yan, A. Stacey, D. A. Simpson, L. T. Hall, D. Maclaurin, S. Prawer, P. Mulvaney, J. Wrachtrup, F. Caruso, R. E. Scholten, L. C. Hollenberg, *Nat. Nanotechnol.* **2011**, *6*, 358.
[194] V. Vaijayanthimala, P. Y. Cheng, S. H. Yeh, K. K. Liu, C. H. Hsiao, J. I. Chao, H. C. Chang, *Biomaterials* **2012**, *33*, 7794.
[195] Y. Kuo, T. Y. Hsu, Y. C. Wu, J. H. Hsu, H. C. Chang, *Proc. SPIE* **2013**, *8635*, 863501.
[196] S. K. Sarkar, A. Bumb, X. Wu, K. A. Sochacki, P. Kellman, M. W. Brechbiel, K. C. Neuman, *Biomed. Opt. Express* **2014**, *5*, 1190.
[197] J. C. Jaskula, E. Bauch, S. Arroyo-Camejo, M. D. Lukin, S. W. Hell, A. S. Trifonov, R. L. Walsworth, *Opt. Express* **2017**, *25*, 11048.
[198] S. Li, X.-d. Chen, B.-W. Zhao, Y. Dong, C.-W. Zou, G.-C. Guo, F.-W. Sun, *Appl. Phys. Lett.* **2016**, *109*, 111107.
[199] M. C. Fischer, J. W. Wilson, F. E. Robles, W. S. Warren, *Rev. Sci. Instrum.* **2016**, *87*, 031101.
[200] A. Leray, J. Mertz, *Opt. Express* **2006**, *14*, 10565.
[201] F. Ganikhanov, C. L. Evans, B. G. Saar, X. S. Xie, *Opt. Lett.* **2006**, *31*, 1872.
[202] C. Zheng, R. Zhou, C. Kuang, G. Zhao, Z. Yaqoob, P. T. So, *Opt. Lett.* **2017**, *42*, 1448.
[203] A. Leray, C. Odin, E. Huguet, F. Amblard, Y. L.e Grand, *Opt. Commun.* **2007**, *272*, 269.

© 2020 Wiley-VCH GmbH

[204] P. Campagnola, *Anal. Chem.* **2011**, *83*, 3224.
[205] K. H. Matlack, J. Y. Kim, L. J. Jacobs, J. Qu, *J. Nondestruct. Eval.* **2015**, *34*, 273.
[206] J. Butet, P.-F. Brevet, O. J. F. Martin, *ACS Nano* **2015**, *9*, 10545.
[207] T. Gottschall, T. Meyer, M. Baumgartl, C. Jauregui, M. Schmitt, J. Popp, J. Limpert, A. Tuennermann, *Laser Photonics Rev.* **2015**, *9*, 435.
[208] N. Dudovich, D. Oron, Y. Silberberg, *Nature* **2002**, *418*, 512.
[209] O. Burkacky, A. Zumbusch, C. Brackmann, A. Enejder, *Opt. Lett.* **2006**, *31*, 3656.
[210] M. D. Duncan, J. Reintjes, T. J. Manuccia, *Opt. Eng.* **1985**, *24*, 352.
[211] J. X. Cheng, A. Volkmer, L. D. Book, X. S. Xie, *J. Phys. Chem. B* **2001**, *105*, 1277.
[212] L. Li, H. F. Wang, J. X. Cheng, *Biophys. J.* **2005**, *89*, 3480.
[213] M. Zimmerley, C.-Y. Lin, D. C. Oertel, J. M. Marsh, J. L. Ward, E. O. Potma, *J. Biomed. Opt.* **2009**, *14*, 044019.
[214] C. Fang, F. Lu, W. Zheng, Z. Huang, *Opt. Express* **2010**, *18*, 15714.
[215] A. Gasecka, A. Daradich, H. Dehez, M. Piche, D. Cote, *Opt. Lett.* **2013**, *38*, 4510.
[216] C. Silien, N. Liu, N. Hendaoui, S. A. Tofail, A. Peremans, *Opt. Express* **2012**, *20*, 29694.
[217] M. Kumbham, S. Daly, K. O'Dwyer, R. Mouras, N. Liu, A. Mani, A. Peremans, S. M. Tofail, C. Silien, *Opt. Express* **2016**, *24*, 24377.
[218] G. L. Carr, *Rev. Sci. Instrum.* **2001**, *72*, 1613.
[219] A. L. Tchebotareva, P. V. Ruijgrok, P. Zijlstra, M. Orrit, *Laser Photonics Rev.* **2010**, *4*, 581.
[220] L. Wei, W. Min, *Anal. Bioanal. Chem.* **2012**, *403*, 2197.
[221] D. Fu, T. E. Matthews, T. Ye, I. R. Piletic, W. S. Warren, *J. Biomed. Opt.* **2008**, *13*, 040503.
[222] W. Min, S. Lu, S. Chong, R. Roy, G. R. Holtom, X. S. Xie, *Nature* **2009**, *461*, 1105.
[223] S. Chong, W. Min, X. S. Xie, *J. Phys. Chem. Lett.* **2010**, *1*, 3316.
[224] P. Wang, M. N. Slipchenko, J. Mitchell, C. Yang, E. O. Potma, X. Xu, J. X. Cheng, *Nat. Photonics* **2013**, *7*, 449.
[225] G. V. Hartland, *Chem. Sci.* **2010**, *1*, 303.
[226] S. S. Lo, M. S. Devadas, T. A. Major, G. V. Hartland, *Analyst* **2013**, *138*, 25.
[227] N. Liu, M. Kumbham, I. Pita, Y. Guo, P. Bianchini, A. S. A. M. Diaspro, A. Tofail Peremans, C. Silien, *ACS Photonics* **2016**, *3*, 478.
[228] J. Enderlein, *Appl. Phys. Lett.* **2005**, *87*, 094105.
[229] J. Humpolickova, A. Benda, J. Enderlein, *Biophys. J.* **2009**, *97*, 2623.
[230] R. Oketani, A. Doi, N. I. Smith, Y. Nawa, S. Kawata, K. Fujita, *Opt. Lett.* **2017**, *42*, 571.
[231] V. Le, X. N. Wang, C. F. Kuang, X. Liu, *Opt. Commun.* **2018**, *426*, 541.
[232] N. Nunn, M. Torelli, G. McGuire, O. Shenderova, *Curr. Opin. Solid State Mater. Sci.* **2017**, *21*, 1.
[233] M. Fernandez-Suarez, A. Y. Ting, *Nat. Rev. Mol. Cell Biol.* **2008**, *9*, 929.
[234] Y. F. Wang, C. F. Kuang, Z. T. Gu, X. Liu, *Opt. Laser Technol.* **2013**, *48*, 489.
[235] B. R. Boruah, *Appl. Opt.* **2010**, *49*, 701.
[236] W. Huang, Y. H. Zhang, Y. Xiao, F. M. Wang, Y. G. Tang, *Optik* **2018**, *157*, 707.
[237] S. Segawa, Y. Kozawa, S. Sato, *Opt. Lett.* **2014**, *39*, 4529.

Chuankang Li is a Ph.D. candidate in the College of Optical Science and Engineering at Zhejiang University in Hangzhou, Zhejiang, China. He received his M.S. degree in Zhejiang University of Technology in 2013. His research fields are super-resolution microscopy, inorganic fluorescent labels and localization imaging.

Vannhu Le received his M.S and Ph.D. degrees in the Harbin Institute of Technology in 2012 and 2016, respectively. Recently, he is a postdoc in the College of Optical Science and Engineering at Zhejiang University in Hangzhou city, Zhejiang, China. His research fields are fluorescence super-resolution microscopy, wavefront coding systems, imaging processing, and optical design.

© 2020 Wiley-VCH GmbH

Cuifang Kuang received his Ph.D. degrees in school of science of Beijing Jiaotong University in 2007. From June 2007 to January 2008, he was a postdoctoral researcher in Beijing Institute of technology. From February 2008 to February 2010, he was a postdoctoral researcher in Department of Mechanical Engineering in University of South Carolina. From September 2014 to September 2015, he went on an academic visit to Massachusetts Institute of Technology. Now he is a professor in the College of Optical Science and Engineering of Zhejiang University with research interests in optical super-resolution imaging.

© 2020 Wiley-VCH GmbH